T. M. Burgers[1], L. A. Miller[2], S. Rysgaard[1,3,4], J. Mortensen[4], B. Else[5], J.-É. Tremblay[6], and T. Papakyriakou[1]

[1]Centre for Earth Observation Science, Department of Environment & Geography, University of Manitoba, Winnipeg, MB, Canada

[2]Institute of Ocean Sciences, Fisheries and Oceans Canada, Sidney, BC, Canada

[3]Arctic Research Centre, Department of Bioscience, Aarhus University, Aarhus, Denmark

[4]Greenland Climate Research Centre, Greenland Institute of Natural Resources, Nuuk, Greenland

[5]Department of Geography, University of Calgary, Calgary, AB, Canada

[6]Québec-Océan and Takuvik Joint International Laboratory, Départment de Biologie, Université Laval, Québec, QC, Canada

Corresponding author: T. M. Burgers (tonya.burgers@umanitoba.ca)

Key Points:

- Siberian shelf waters are identifiable in Nares Strait, in the high Canadian Arctic Archipelago
- The position of the Transpolar Drift determines surface water properties in Nares Strait, affecting regional productivity and $CO_2$ uptake
- Primary production is limited in Nares Strait due to nutrient-limited surface waters, but plays an important role in lowering surface $pCO_2$

**Abstract**

The water mass assembly of Nares Strait is variable, owing to fluctuating wind forcings over the Arctic Basins, and irregular northward flows from the West Greenland Current (WGC) in Baffin Bay. Here we characterize the physicochemical properties of the water masses entering Nares Strait in August 2014, and we employ an extended optimum multi-parameter (OMP) water mass analysis to estimate the mixing fractions of predefined source water masses, and to distinguish the role of physical and biological processes in governing the distribution of dissolved inorganic carbon (DIC) in Nares Strait. We show the first documented evidence of Siberian shelf waters in Nares Strait, along with a diluted upper halocline layer of partial Pacific-origin. These mixed-origin water masses appear to play an important role in driving a modest phytoplankton bloom in Kane Basin, leading to decreased surface $pCO_2$ concentrations in Nares Strait. Although inorganic nitrogen was already limited in the surface mixed layer in northern Nares Strait, the unique properties of mixed Atlantic-Pacific water facilitated upwelling and nutrient supply to the surface. These observations suggest that the positioning of the Transpolar Drift, and hence the balance of Atlantic and Pacific water delivered to Nares Strait, is likely to play an important role in regional biological productivity and carbon uptake from

the atmosphere. We also observed water masses from the WGC transported as far north as Kane Basin, contributing to relatively high $pCO_2$ and low pH in the intermediate and deep water column of southern Nares Strait and northern Baffin Bay.

**Plain Language Summary**

Nares Strait is the northernmost outflow channel of the Arctic Ocean, located between Ellesmere Island and northern Greenland. The physical and chemical properties of the waters exiting the Arctic Ocean through Nares Strait play an important role in freshwater transport, carbon dynamics, and in supplying nutrients to marine ecosystems downstream, including delivery to the historically productive North Water polynya region. The water masses transported through Nares Strait are known to change depending on the predominant wind patterns over the Arctic Ocean. Here we document the export of surface waters that originated from the Siberian shelf seas, on the other side of the Arctic Ocean, carrying with them a strong river water signal. We also capture the northward transport of water from eastern Baffin Bay into Nares Strait. This study demonstrates that the carbon dynamics in Nares Strait are largely dictated by mixing of water masses from the north and south, although local biology plays an important role in facilitating $CO_2$ drawdown in Nares Strait and further downstream.

## 1 Introduction

The many channels of the Canadian Arctic Archipelago (CAA) represent an important export pathway for Arctic outflow waters and the transport of freshwater to the North Atlantic (Carmack et al., 2016). Located between Ellesmere Island and Greenland, Nares Strait is the northernmost outflow gateway of the Arctic Ocean, and one of two main passages through the CAA (Figure 1). Nares Strait connects the Lincoln Sea, an ice-covered continental shelf sea, with northern Baffin Bay, which harbors the ecologically significant North Water (NOW) polynya, or *Pikialasorsuaq* in Greenlandic (Eegeesiak et al., 2017). Nares Strait is largely a flow-through system, transporting Arctic waters southwards through a series of channels and basins, which from north to south are: Robeson Channel, Hall Basin, Kennedy Channel, Kane Basin, and finally Smith Sound (Figure 1a). The net southward volume transport through Nares Strait is estimated to be 0.8 ± 0.3 Sv, approximately equal to the net volume flux of Pacific water into the Arctic Ocean via Bering Strait (Münchow et al., 2006). In Kane Basin the seafloor shallows to a minimum sill depth of 220 m, allowing only a portion of deep Atlantic-origin waters to be exported from the Arctic Ocean.

Previous studies have shown that the region north of the Lincoln Sea acts as a switchyard, directing either Pacific- or Atlantic-origin surface waters towards the Lincoln Sea and Nares Strait depending on the predominant atmospheric circulation patterns and the location of the Transpolar Drift (TPD; Jackson et al., 2014; Newton & Sotirin, 1997; Steele et al., 2004; de Steur et al., 2013). The TPD is a surface current of water and sea ice that forms at the intersec-

tion of two gyres in the central Arctic Ocean: the anticyclonic Beaufort Gyre that dominates the surface circulation of the Amerasian Basin; and the cyclonic circulation over the Eurasian Basin (Figure 1b). The position of the TPD has been found to vary, from being roughly aligned with the Lomonosov Ridge during periods of predominantly anticyclonic circulation (an expanded Beaufort Gyre; negative Arctic Oscillation index), to beginning closer to the Chukchi shelf, spreading along the Mendeleyev Ridge during periods of predominantly cyclonic circulation (a contracted Beaufort Gyre; positive Arctic Oscillation index) (Morison et al., 2012; Steele et al., 2004). The spread of Pacific waters into the central Arctic Ocean is dependent on the expansion versus the contraction of the Beaufort Gyre, and thus the orientation of the TPD also largely determines the location of the Pacific/Atlantic front (Alkire et al., 2021). Steele et al. (2004) reported a connection between the onset of a positive Arctic Oscillation (AO) index in the early 1990's and the arrival of relatively warm (temperature of $-1.2$ °C) summer Pacific waters in the Lincoln Sea, following an approximately 3-year time lag. Later deSteur et al. (2013) reinforced these findings, also noting large freshwater anomalies in the Lincoln Sea coinciding with the arrival of summer Pacific waters, but found the time lag could vary from zero to 3 years. Other recent studies in the Lincoln Sea and Nares Strait have documented significant interannual variability in the water mass assembly, with inputs from both the Amerasian (Pacific-influenced) and Eurasian (Atlantic-influenced) basins (Alkire et al., 2010; Hamilton et al., 2021; Jackson et al., 2014; Münchow et al., 2007). Depending on the configuration of the TPD, in any particular year the Lincoln Sea (and Nares Strait) may receive surface waters from the west Siberian shelves (Atlantic-origin) or the Chukchi shelf (Pacific-origin). The influence of this "switchyard effect" (the changing positioning of the TPD) on the waters transported through Nares Strait has not been studied, and may have implications for the export budgets of freshwater and carbon from the Arctic Ocean.

The Lincoln Sea is also the location of the Last Ice Area, the region where multiyear sea ice is expected to persist longest in the face of climate change (Moore et al., 2019). Historically, the formation of an ice arch at Smith Sound has contributed to both the longevity of the Last Ice Area and the formation of the NOW polynya. However, since the 1990s the timing and location of the ice arch has become increasingly variable, with the ice arch forming later, breaking up earlier, and occasionally forming farther north, at the boundary between Nares Strait and the Lincoln Sea (Figure 1a; Vincent, 2019). When the ice arch is not present the southerly flow of sea ice through Nares Strait can substantially decrease downstream salinity in the Labrador Sea (Barber et al., 2018; Kwok et al., 2010) and increases the export of multiyear sea ice from the Last Ice Area (Moore et al., 2019; Ryan & Münchow, 2017). This can also have negative consequences for annual primary production in the NOW polynya region, as thick multiyear sea-ice floes shade the upper water column, limiting light availability for phytoplankton (Blais et al., 2017; Marchese et al., 2017).

The NOW polynya region in northern Baffin Bay has its own unique water

column characteristics, governed by the convergence of Arctic outflow waters from Nares Strait with a separate water mass assembly transported northwards by the West Greenland Current (WGC) from the subpolar North Atlantic (Bâcle et al., 2002; Lobb et al., 2003; Melling et al., 2001; Mortensen et al., 2022; Rysgaard et al., 2020). At the front where these two water mass assemblies meet, cross-frontal gradients in temperature and salinity have been found to be largely density compensating, leading to a high degree of isopycnal interleaving (Lobb et al., 2003). The complex bathymetry of the NOW region plays a key role in directing the interaction of these water mass assemblies, as the majority of WGC waters follow the 600 m isobath westwards across northern Baffin Bay without entering the NOW polynya region. A smaller portion of the WGC follows the 400 m isobath entering the NOW region from the southeast, and has been observed as far north as Smith Sound where it is forced southwards again by the shoaling bathymetry (Melling et al., 2001). Sporadic net northerly flows have been documented across Smith Sound, but the frequency of these events is not regular and the forcings that drive them are only just beginning to be understood (Melling et al., 2001; Münchow et al., 2015; Myers et al., 2021). For example, Myers et al. (2021) recently linked a month-long net transport reversal in Baffin Bay and Nares Strait to an anomalous wind pattern along West Greenland.

Variability in the water mass assembly and sea-ice cover in Nares Strait have implications for freshwater and nutrient budgets, and for biogeochemical processes such as air-sea $CO_2$ exchange, primary production, and ocean acidification. This water mass variability impacts not only the biogeochemistry of Nares Strait, but also that of ecologically important downstream regions such as the NOW polynya. Despite the importance of Nares Strait as a conduit connecting the greater Arctic Ocean to northern Baffin Bay and ultimately the North Atlantic, very little is known about the biogeochemical processes occurring within these waters, nor about the transport and distribution of dissolved carbon. A former study, using a portion of the data presented here, identified relatively high surface $CO_2$ partial pressure ($pCO_2$) coinciding with a strong riverine signal in Nares Strait in August 2014 (Burgers et al., 2017). This study builds on those initial findings by investigating the water mass assembly that was present in Nares Strait at that time. Here we employ an extended optimum multi-parameter (eOMP) analysis to characterize and trace the various water masses transiting through Nares Strait, and to distinguish the impacts of physical (water mass transport) and biological processes on the observed distribution of dissolved inorganic carbon (DIC). The objectives of this study were to investigate: (1) the origins of the water masses observed in Nares Strait, (2) the carbonate chemistry and nutrient concentrations of these water masses, and (3) the biogeochemical processes occurring within Nares Strait that affect the observed water column distribution of DIC. Finally, we will put our results in context by describing the possible variability in the water mass assembly of Nares Strait that may affect the future carbon dynamics and primary production in this region.

## 2 Data and Methods

### 2.1 Setting

Sampling for this study was conducted during the 2014 ArcticNet scientific cruise onboard the Canadian icebreaker CCGS *Amundsen,* starting with an east-to-west transect of stations across the NOW region from 30 July to 1 August (stations 115 to 101, Figure 1a). The *Amundsen* then transited north in Nares Strait before completing a north-to-south series of stations from the northern end of Kennedy Channel (station Ken1) on 3 August back into the NOW region of northern Baffin Bay (station 120) on 6 August (see Table S1 for sampling times and exact locations). At the time of sampling the NOW polynya ice arch remained present at the northern end of Kennedy Channel, causing sea ice concentrations to remain above 90% north of 81.5 °N, with mainly open waters southwards where our sampling was conducted (Figure 1a).

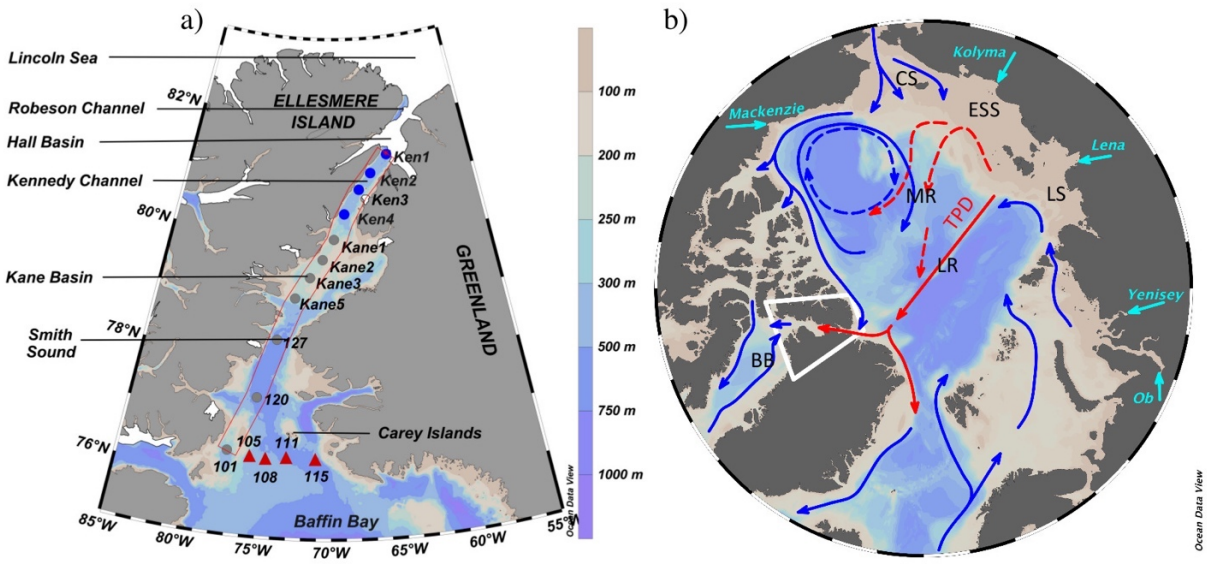


Figure 1: (a) Map of the study area, with water column sampling stations indicated as coloured dots, and the Nares Strait transect referred to throughout the text indicated by a red outline. Stations plotted as blue dots indicate the northern source region, while stations plotted as red triangles indicate the southern source region, relevant to our eOMP analysis (see section 2.4), stations plotted as grey dots represent the mixing region between the two source regions. Areas where sea-ice concentrations were >90% at the time of sampling are shaded white, based on weekly ice charts from the Canadian Ice Service. (b) Map of the Arctic Ocean with major surface circulation features (arrows), including the Transpolar Drift (TPD; red arrows). Solid and dotted lines indicate the position of these features during a negative and positive Arctic Oscillation index, respec-

tively. Outflow locations of major Arctic rivers are shown in cyan, with the current study area outlined in white. Abbrevations: Baffin Bay (BB), Laptev Sea (LS), East Siberian Sea (ESS), Chukchi Sea (CS), Lomonosov Ridge (LR), Mendeleyev Ridge (MR), Transpolar Drift (TPD). Maps created using Ocean Data View software (Schlitzer, 2020).

2.2 Sampling and sample analyses

At each sampling station seawater was collected with 12L Niskin-type bottles mounted on a rosette system equipped with a SeaBird 911plus CTD, as well as sensors for chlorophyll fluorescence (SeaPoint), dissolved oxygen (Seabird SBE-43), and fluorescent colored dissolved organic matter (*f*CDOM, WetLabs ECO). Salinity is reported using the practical salinity scale 1978 (PSU). The oxygen sensor was calibrated onboard against Winkler titrations, and the chlorophyll concentrations from the fluorescence probe were calibrated from extracted Chl *a* (Amundsen Science Data Collection, 2018). The *f*CDOM units are relative from factory calibrations. Discrete water samples were collected for the analysis of nutrients (including nitrate, nitrite, ammonium, phosphate, and silicate), and the inorganic carbon system (dissolved inorganic carbon [DIC] and total alkalinity [TA]). Discrete samples were collected at standard depths of: 2, 10, 20, 30, 40, 50, 60, 70, 80, 100, 125, 150, 175, 200, 250, and 300 m with any depths greater than 300 m being sampled at 100 m intervals to a maximum depth of 10 m above the sea floor. If required an additional sampling depth was added at the chl-*a* maximum. At some stations DIC/TA samples were only collected at the surface and 10 m depth; stations with full DIC/TA profiles are indicated in Table S1.

Nutrient samples were collected directly from the Niskin-type bottles with syringes, filtered in-line (Swinnex-mounted, Whatman GF/F), and captured in acid-cleaned polyethylene tubes. Nutrient concentrations for nitrate+nitrite, ammonium, phosphate, and silicate were measured colorimetrically with a Bran and Luebbe AutoAnalyzer III (Hansen & Koroleff, 1999) within a few hours of collection onboard the ship. Analytical detection limits were 0.03 µM for nitrate, 0.02 µM for nitrite, 0.05 µM for phosphate, and 0.1 µM for silicate. Ammonium concentrations were measured using the method of Holmes et al. (1999) with a detection limit of 0.02  M.

Seawater samples for analysis of the carbon dioxide system were collected and analyzed following standard protocols (Dickson et al., 2007). Samples were collected in 250-mL glass bottles, preserved with 100 µL of saturated mercuric chloride solution, capped with ground glass stoppers greased with Apiezon M, and sealed with electrical tape. Replicates were collected from at least one Niskin-type bottle per rosette cast. Samples were then stored in the dark at 4℃ until arrival and analysis at the Institute for Ocean Sciences in Sidney, British Columbia, within 10 months of collection. The coulometric DIC analysis utilized either a SOMMA or VINDTA 3D (MARIANDA) extraction system. Measurements of TA used open-cell potentiometric titrations with nonlinear least squares end-point determination. Both of these measurements were calibrated

against certified reference materials (CRM batches 88, 115, and 133, provided by Andrew Dickson, Scripps Institute of Oceanography). Analyses of duplicate DIC and TA samples indicate a precision of ± 1 µmol $kg^{-1}$ and ± 3 µmol $kg^{-1}$, respectively. Following the determination of DIC and TA, we calculated in-situ pH on the total scale ($pH_T$), the partial pressure of $CO_2$ ($pCO_2$), aragonite saturation state ($\Omega_{Ar}$), and calcite saturation state ($\Omega_{Ca}$) using the MATLAB $CO_2$Sys program of van Heuven et al. (2011) with the uncertainty propagation routine of Orr et al. (2018). Within $CO_2$Sys we applied the carbonic acid dissociation constants of Lueker et al. (2000), the $HSO_4^-$ dissociation constants of Dickson (1990), and the total boron concentration from Lee et al. (2010).

Additionally, continuous sea surface measurements of $pCO_2$ were collected using an underway system (General Oceanics model 8050; Pierrot et al., 2009), which sampled from a seawater intake line at a nominal depth of 7 m. The system's infrared gas analyzer (LI-COR LI-7000) was calibrated twice daily against three certified gas standards traceable to World Meteorological Organization (WMO) standards. The relative uncertainty of the resulting $pCO_2$ measurements is estimated to be 2%; see Burgers et al. (2017) for further information about the underway $pCO_2$ system and data processing.

### 2.3 Geochemical tracers

Due to active sedimentary denitrification over the Chukchi shelf, inflowing Pacific-source waters to the Arctic Ocean exhibit a lower nitrogen-phosphate (N-P) ratio compared to inflowing Atlantic waters from Fram Strait and the Barents Sea. Following Newton et al. (2013), we calculated the "Arctic N-P" tracer (ANP) which exploits this difference in N-P ratio to estimate the amount of Pacific-source water contained in a sample. In calculating ANP we applied the N-P regression lines of Pacific and Atlantic waters from Yamamoto-Kawai et al. (2008) to our measurements of total inorganic nitrogen (TIN = $NO_3^-$ + $NO_2^-$, + $NH_4^+$) and phosphate ($PO_4^{3-}$). The regression lines of Yamamoto-Kawai et al. were defined using measurements of TIN, like ours, instead of solely nitrate concentrations (e.g. Jones et al., 1998). If ANP=0, the TIN-P pair falls along the Atlantic water regression line, whereas if ANP=1, the TIN-P pair falls along the Pacific water line. However, the Chukchi shelf is not the only shelf sea of the Arctic Ocean where denitrification can occur. Denitrification has also been documented in the shelf sediments of the East Siberian and Laptev Seas (Bauch et al., 2011; Nitishinsky et al., 2007). Hence, ANP values greater than 0 do not definitively indicate Pacific source waters, as Atlantic source waters may also undergo denitrification in the Siberian shelf seas. Alkire et al. (2019, 2021) have proposed using the NO parameter as a qualitative tracer for distinguishing waters from the Chukchi and Siberian shelf seas. NO is a quasi-conservative tracer, defined as: $NO = 9[NO_3^-] + [O_2]$ (Broecker, 1974), that can be used to trace water masses at depths below the surface mixed layer. Since nitrate and oxygen concentrations are generally higher in the Chukchi Sea compared to the Siberian shelf seas, NO is generally higher in waters originating from the Chukchi ($> 400$ µmol $kg^{-1}$) compared to the Siberian shelf seas ($< 400$ µmol

$kg^{-1}$; Alkire et al., 2021). Hence, NO can be a useful tool in distinguishing these two shelf waters, both of which may ventilate the upper halocline layer within the Amerasian basin of the Arctic Ocean.

### 2.4 eOMP analysis

In this investigation we utilize the extended optimum multiparameter (eOMP) analysis of Dinauer & Mucci (2018), which estimates both the mixing fractions of predefined source water masses, and the impact of biological processes (photosynthesis/respiration) that best reproduce the observed tracer measurements. The base MATLAB code for the eOMP analysis was provided by Ashley Dinauer (Universität Bern), and is described in detail in Dinauer & Mucci (2018). We have also made some modifications to the method of Dinauer & Mucci, which will be outlined later in this section. Briefly, OMP analysis is a weighted, non-negative, linear inverse mixing model that optimizes the information contained in a hydrographic dataset. OMP analysis calculates the best fitting fractions ($f$) of ($n$+1) source water masses that contribute to the ($n$) observed tracer measurements in a parcel of water by solving an over-determined system of linear equations that minimizes residual error (Tomczak & Large, 1989; Tomczak, 1981). The *extended* OMP (eOMP) method employed here also includes a biological term which estimates tracer concentration changes due to the impact of net photosynthesis or net respiration within the water column. The eOMP method of Dinauer & Mucci employs the measure of apparent oxygen utilization (AOU) to predict the biogeochemical regime (either net photosynthesis or net respiration), at any given measurement point. When AOU $> 0$ we assume that community respiration exceeds photosynthesis (net respiration), releasing DIC and nutrients into the water column while consuming oxygen. When AOU $< 0$ we assume that the rate of photosynthesis exceeds community respiration, with phytoplankton consuming DIC and nutrients while releasing oxygen. Therefore, whether AOU is positive or negative at any given measurement point determines the sign of the Redfield ratios in equation 1 (below).

We employ the eOMP framework with nine physicochemical tracers: potential temperature ( ), salinity (S), dissolved oxygen (DO), phosphate (P), total inorganic nitrogen (TIN), silicate (Si), total alkalinity (TA), dissolved inorganic carbon (DIC), and fluorescent colored dissolved organic matter ($f$CDOM). The equations applied in this eOMP framework are:

$$
\begin{aligned}
&f_1\theta_1 + ... + f_n\theta_n + 0 = \theta_{\text{obs}} + R_\theta \qquad (1)\\
&f_1 S_1 + ... + f_n S_n + 0 = S_{\text{obs}} + R_S\\
&f_1\text{DO}_1 + ... + f_n\text{DO}_n \pm\ r_{DO/P}\ P =\\
&\text{DO}_{\text{obs}} + R_{\text{DO}}\\
&f_1 P_1 + ... + f_n P_n \pm\ r_{P/P}\ P = P_{\text{obs}} + R_P\\
&f_1\text{TIN}_1 + ... + f_n\text{TIN}_n \pm\ r_{N/P}\ P =\\
&\text{TIN}_{\text{obs}} + R_{\text{TIN}}\\
&f_1\text{Si}_1 + ... + f_n\text{Si}_n \pm\ r_{Si/P}\ P =\\
&\text{Si}_{\text{obs}} + R_{\text{Si}}\\
&f_1\text{TA}_1 + ... + f_n\text{TA}_n \pm\ r_{N/P}\ P =\\
&\text{TA}_{\text{obs}} + R_{\text{TA}}\\
&f_1\text{DIC}_1 + ... + f_n\text{DIC}_n \pm\ r_{C/P}\ P =\\
&\text{DIC}_{\text{obs}} + R_{\text{DIC}}\\
&f_1\text{CDOM}_1 + ... + f_n\text{CDOM}_n + 0 =\\
&\text{CDOM}_{\text{obs}} + R_{\text{CDOM}}\\
&f_1 + ... + f_n + 0 = 1 + R_{\text{mass}}
\end{aligned}
$$

where $f$ indicates the calculated mixing fractions of $n$ source water masses, which compose the observed tracer fields through conservative mixing. Subscripts on variable names (e.g., $S_n$, $TIN_n$, etc.) indicate the defined source water mass concentrations (see Table 1). On the right-hand side of the equations, *obs* terms represent observed tracer concentrations, and $R$ are residual terms of each tracer. For the biological change term we employ Redfield-type ratios relative to phosphate ($r_{\text{tracer/P}}$). The eOMP model calculates the term $\Delta$P, representing the change in phosphate concentration due to biological processes. The multiplication of $\Delta$P by the appropriate Redfield ratio for each tracer estimates the concentration change of that tracer due to biological activity. Following Dinauer & Mucci (2018) we applied the traditional C:-$O_2$ Redfield ratio of 106:-138, whereas we estimated the local TIN:P and Si:P ratios for Nares Strait. To do this we utilized linear regressions of nutrient data throughout the upper water column (S  33.2) at our two most northerly stations, where surface waters had just emerged from under thick ice cover, and measurements of chlorophyll-*a* fluorescence were less than 1 mg $m^{-3}$ (see Figure S1 for linear regressions). The TIN:P ratio from this analysis was 11:1, which is somewhat lower than the classical Redfield ratio, but this is typical of Arctic surface waters (Tremblay et al., 2015), and the Si:P ratio was 20:1, which also agrees well with ratios previously reported in Canadian Arctic waters (Tremblay et al., 2002, 2015).

The first step in our eOMP analysis is to define the source water masses that contribute to the water mass assembly in Nares Strait and the NOW region. For biogeochemical OMP studies it is important that each source water mass be defined at the location where it enters the region of interest. This allows for the assumption that observed tracer concentrations "downstream" result from the mixing and biological processes occurring within the study region. Nares Strait and the NOW region are influenced by two water mass assemblies, one

arriving from the Arctic Ocean and flowing southwards through Nares Strait, and a second entering from the southeast NOW region and flowing northwards with a branch of the WGC. Following this, two "source regions" were designated where water masses may enter the study region: (1) the northern source region which encompasses our four most northerly stations in Kennedy Channel (represented by the blue stations in Figure 1a); and (2) the southern source region, which includes the four easternmost stations across the NOW region of northern Baffin Bay (red stations in Figure 1a). Water masses in each source region were identified by their unique physicochemical characteristics (e.g., temperature minimum, nutrient maximum,…). We identified three water masses arriving from the northern source region: Polar Mode water (PMW), Upper Halocline water (UHW), and Canada Basin Atlantic water (CBAW); and another two source water masses arriving from the southern source region: Baffin Bay Polar water (BBPW) and Subpolar Mode water (SPMW) (Mortensen et al., 2022; Rysgaard et al., 2020). The specific properties and origins of each source water mass is described in section 3.1. We additionally included two freshwater sources in our eOMP analysis, river runoff (RR) and sea ice melt (SIM), with their definitions derived from literature values (see Table 1 for all source water mass definitions). Tracer concentrations for the RR definition were taken from Charette et al. (2020), who reported linear regression relationships between meteoric water fractions and tracer concentrations in the surface waters of the TPD. Since the major Siberian rivers exert a stronger influence on the TPD than North American rivers (Bauch et al., 2011; Morison et al., 2012), our RR definition is representative of discharge weighted average concentrations from Siberian rivers (Charette et al., 2020). In some cases where tracer concentrations could not be extrapolated to 100% meteoric water without high uncertainty, we utilized tracer concentrations at 20% meteoric water, representing an effective shelf end-member concentration at the point of origin to the TPD (Charette et al. 2020).

Table 1: Defined properties of source water masses employed in eOMP analysis[a]. Source water masses include Polar Mode water (PMW), Upper Halocline water (UHW), Canada Basin Atlantic water (CBAW), Baffin Bay Polar Water (BBPW), and Subpolar Mode water (SPMW). Freshwater sources include sea-ice melt (SIM) and river runoff (RR).

| | **Source water masses** | | | | **Freshwater sources** |
|---|---|---|---|---|---|
| **Property** | **PMW** | **UHW** | **CBAW** | **BBPW** | **SPMW[b]** |
| Temp (°C) | -1.6 ± 0.04 | -1.3 ± 0.02 | 0.36 ± 0.03 | -1.2 ± 0.2 | 2.0 |
| Salinity | 31.4 ± 0.3 | 33.2 ± 0.1 | 34.8 ± 0.1 | 33.5 ± 0.1 | 34.3 |
| DO (µmol $kg^{-1}$) | 360 ± 2 | 290 ± 2 | 270 ± 5 | 310 ± 23 | 220 |
| P (µmol $kg^{-1}$) | 0.70 ± 0.04 | 1.10 ± 0.05 | 0.88 ± 0.01 | 0.78 ± 0.07 | 1.10 |
| TIN (µmol $kg^{-1}$) | 3.5 ± 0.3 | 9.6 ± 0.3 | 13 ± 1 | 7.9 ± 0.6 | 14 |
| Si (µmol $kg^{-1}$) | 9.2 ± 0.7 | 17 ± 1 | 8.0 ± 0.2 | 7.7 ± 0.9 | 17 |
| DIC (µmol $kg^{-1}$) | 2130 ± 6 | 2190 ± 9 | 2170 ± 10 | 2130 ± 6 | 2190 |
| TA (µmol $kg^{-1}$) | 2230 ± 10 | 2260 ± 10 | 2300 ± 6 | 2230 ± 20 | 2260 |

| | Source water masses | Freshwater sources | | | |
|---|---|---|---|---|---|
| $f$CDOM (mg m$^{-3}$) | 11 ± 0.3 | 8.2 ± 0.2 | 4.5 ± 0.1 | 4.4 ± 0.4 | 4.9 |

[a] The defined properties of each source water mass (average ± one standard deviation) were derived from our dataset, and freshwater properties were defined from literature values, see the following footnotes.

[b] SPMW properties are defined at the subsurface temperature maximum of station 115 (Figure 1a)

[c] Östlund & Hut (1984)

[d] Rysgaard et al. (2008)

[e] Mundy et al. (2011)

[f] Rysgaard et al. (2007); Miller et al. (2011)

[g] Concentrations extrapolated to 100% meteoric water from Charette et al. (2020)

[h] Concentrations at 20% meteoric water in the surface TPD from Charette et al. (2020)

Within the eOMP framework the applied tracers are normalized and weighted to allow comparison of otherwise incommensurable parameters, and to account for environmental variability and measurement errors. In this study we have chosen to apply separate weighting schemes in the upper (S < 33.2) and deep (S 33.2) water column, following Lansard et al. (2012). This allows the flexibility to apply lower weights to temperature-sensitive or non-conservative tracers (e.g., , DO, TIN) within the upper water column, where they may be affected by non-conservative processes such as primary production and atmospheric interaction, but increase their weighting at depth where these tracers approach more conservative behaviour. Weights were chosen for the upper and lower water column somewhat objectively, with consideration of the range and precision of each tracer, as well as how conservatively they behave (see Table 2 for assigned weights). In surface waters S was assigned the highest weighting because it is both conservative and precise. The lowest weightings were applied to and DO as they are influenced by large temperature swings by solar insolation near the surface, as well as influences by biological processes for DO. TIN and P were also assigned low weightings due to their biologically-influenced non-conservative behavior. DIC, Si, and $f$CDOM were assigned intermediate weights, as they are non-conservative in surface waters ($f$CDOM photochemically degrades, and DIC and Si are biologically impacted), but they have a high range-to-precision ratio and are powerful tracers for distinguishing water masses in the upper water column. TA was also assigned an intermediate weighting in surface waters as it is a near-conservative parameter, and has a lower analytical precision. Weightings applied in the deep water column increased for , DO, Si,

DIC, TA, and fCDOM, as these tracers approach more conservative behaviour away from the atmosphere-ocean interface.

Table 2: Weights applied to each tracer used in the eOMP analysis, as well as the analytical precision of each tracer measurement, and the median residual term of each tracer after running the eOMP analysis.

| | | Weights in OMP analysis | | |
|---|---|---|---|---|
| Parameters | Analytical precision | Surface (S < 33.2) | Deep (S 33.2) | Median eOMP r |
| Temperature (°C) | 0.01 | 1 | 25 | 0.08 |
| Salinity | 0.01 | 25 | 25 | 0.03 |
| Oxygen (µmol $kg^{-1}$) | 1 | 1 | 2 | 0.5 |
| Phosphate (µmol $kg^{-1}$) | 0.05 | 2 | 2 | 0.01 |
| TIN (µmol $kg^{-1}$) | 0.03 | 2 | 2 | 0.4 |
| Silicate (µmol $kg^{-1}$) | 0.1 | 10 | 20 | 0.3 |
| DIC (µmol $kg^{-1}$) | 1 | 7 | 10 | 8.0 |
| TA (µmol $kg^{-1}$) | 3 | 10 | 15 | 16.7 |
| *f*CDOM (ppb) | 0.09 | 7 | 10 | 0.12 |

*Values in this column represent the median residual term, $R_{tracer}$, for each tracer from equation (1)

The base MATLAB code of Dinauer and Mucci (2018) was also modified to perform separate eOMP runs for the surface and deep water column, only taking into consideration certain source water masses in each domain. This was necessary since not all tracers were sampled at all depths, leading to constraints on the number of source water mass fractions that could be solved for at each sampling depth. Within the surface domain deep and saline (S > 34) source water masses were excluded (i.e., CBAW and SPMW in Table 1). In the deep eOMP run, the freshwater inputs were excluded along with the shallow and fresh (S < 32) PMW (Table 1) source water mass, which is confined to the upper 100 m of the water column. Taking this approach still produces realistic results because of the strong salinity stratification in this region, which limits mixing between the upper and lower water column, and certain water masses that are present at the interface between these two domains (e.g. UHW and BBPW) are still calculated for in both the surface and deep domains.

We performed a sensitivity analysis of this eOMP framework, to assess how robust the calculated water mass fractions are with regards to: (1) the applied weightings for each tracer; and (2) the natural variability of each source water mass definition. We did this by completing multiple eOMP runs while varying the applied tracer weights by +/- 10 (up to a maximum of 25, or down to a minimum of 1), and by varying the source water mass definitions by one standard deviation (see Table 1 for source water mass definitions). The results of these sensitivity analyses are presented in Figures S2 to S4 in the supplemental materials and demonstrate that the results of our eOMP analysis are quite stable.

Generally, changes in calculated water mass fractions were under 0.1 (or 10%). The one exception where we found higher sensitivity is in calculated fractions of PMW and BBPW (up to 50%) within the surface domain (Figure S2). The eOMP framework has trouble discriminating these two water masses near the surface when certain tracer weightings are altered, specifically non-conservative tracers such as DO, P, TIN, Si, and CDOM. Therefore, we find that calculated fractions of PMW and BBPW within the surface domain are affected by the highest uncertainties. A more detailed discussion of our sensitivity analysis is included in the supplementary information (Text S1). Another indicator of the uncertainty associated with our eOMP analysis is shown by the calculated residual terms ($R$) of each tracer. Table 2 includes the median residual terms for each applied tracer, with the median mass conservation residual being 0.3% (total range of 0.1% to 4.5%). Since multiple sources of error exist in the application of eOMP (e.g., source water mass definition error, measurement errors), the mass conservation residual will never be zero, but the fact that our mass conservation residuals do not exceed 5% indicates that the source water masses considered in our model replicate the observed water mass properties well (Dinauer & Mucci, 2018).

2.5 Inorganic carbon budget

The combined effects of water mass mixing, biological activity, and air-sea gas exchange on the observed DIC field are summarized by the following budget:

$$\mathrm{DIC}_{\mathrm{obs}} = \mathrm{DIC}_{\mathrm{mix}} + \mathrm{DIC}_{\mathrm{bio}} + DIC_{\mathrm{gas}} \quad (2)$$

where $\mathrm{DIC}_{\mathrm{obs}}$ is the observed value, $\mathrm{DIC}_{\mathrm{mix}}$ is the DIC concentration resulting from water mass mixing, $\Delta\mathrm{DIC}_{\mathrm{bio}}$ is the change in DIC concentration due to either net photosynthesis or respiration, and $\Delta\mathrm{DIC}_{\mathrm{gas}}$ represents either the addition or loss of DIC due to $CO_2$ gas exchange with the atmosphere. The $\mathrm{DIC}_{\mathrm{mix}}$ and $\Delta\mathrm{DIC}_{\mathrm{bio}}$ terms in this budget are derived from our eOMP model output, as:

$$\mathrm{DIC}_{\mathrm{mix}} = f_1\mathrm{DIC}_1 + ... + f_n\mathrm{DIC}_n \quad (3)$$

$$DIC_{\mathrm{bio}} = \pm r_{C/P}\, P \quad (4)$$

However, the $\mathrm{DIC}_{\mathrm{gas}}$ term is not directly accounted for within the eOMP framework. This term is more difficult to accurately estimate, as biological processes and mixing are likely to have a larger influence over relatively short timescales. At the time of our sampling in Nares Strait an ice-arch remained present north of Kennedy Channel, meaning surface waters had only recently come into contact with the atmosphere after emerging from a consolidated sea ice cover. We take advantage of this unique setting to calculate the $\mathrm{DIC}_{\mathrm{gas}}$ term as the time-integrated flux of carbon into the surface mixed layer for each of the eleven

sampling stations in the Nares Strait transect (see Figure 1a for transect location) since the estimated time that sampled parcel of water emerged from under the ice-arch in northern Kennedy Channel. We assume that the surface flow in Nares Strait is predominantly southwards, until arriving in the NOW polynya region, which is known to be strongly influenced by waters from the WGC (Melling et al., 2001; this will also be demonstrated in section 3.2) and would have a longer history of atmospheric interaction. Therefore, we do not calculate the $DIC_{gas}$ term for stations in our southern source region (see Figure 1a).

We calculate the $DIC_{gas}$ term by utilizing underway $pCO_2$ measurements, and wind speeds from the North American Regional Reanalysis (NARR), to calculate a time-integrated flux of carbon into the surface mixed layer for each of the sampling stations in our Nares Strait transect. We assume that the observed spatial pattern in surface water $pCO_2$ would remain roughly constant throughout the summer season, and that surface waters in Nares Strait travelled at an average southward speed of 15 cm $s^{-1}$ (Münchow, 2016). Assuming this constant current speed, we can estimate the date and time at which a water parcel emerged from the northern ice arch, before arriving at its sampled station location downstream. Following this procedure, the $DIC_{gas}$ term is calculated as:

$$DIC_{gas} = \frac{\int_{t_1}^{t_2} -F_{gas}}{\overline{MLD} \bullet \rho_{MLD}} \quad (5)$$

Where $F_{gas}$ is the air-sea $CO_2$ flux (µmol C $m^{-2}$ $day^{-1}$; positive upward, from ocean to atmosphere) associated with each underway $pCO_2$ measurement, $t_1$ is the estimated time that a sampled water parcel departed the ice arch, and $t_2$ is the time it was sampled downstream. $\overline{MLD}$ is the mean surface mixed layer depth (10 m in Nares Strait during our study), and $_{MLD}$ is the mean surface mixed layer density at each station. Briefly, $F_{gas}$ was calculated from the gas transfer velocity ($k$) parameterized following Wanninkhof (2014) employing NARR wind speeds, the $CO_2$ solubility ( ) at in-situ temperature and salinity (Weiss, 1974), and the difference in the $CO_2$ partial pressures between the surface water and atmosphere ($\Delta pCO_2 = pCO_{2sw} - pCO_{2atm}$). Atmospheric $CO_2$ measurements were collected using a closed-path infrared gas analyzer (LI-COR model LI-7000) with an intake located at a height of 13 m above sea level on a meteorological tower on the ship's foredeck. $F_{gas}$ was calculated as:

$$F_{gas} = \alpha k(\ pCO_2), \quad (6)$$

When calculating $DIC_{gas}$ we integrated the negative of $F_{gas}$ over time, so that positive $DIC_{gas}$ values represent oceanic uptake of $CO_2$ from the atmosphere,

and negative $DIC_{gas}$ values indicate $CO_2$ loss to the atmosphere. Further details on the calculation of $DIC_{gas}$ are provided in Text S2. We estimate the relative uncertainty of the $DIC_{gas}$ term to be 20 – 30% based on the propagation of uncertainties associated with the gas transfer velocity (approximately 20% relative uncertainty; Wanninkhof, 2014), and the uncertainty of our underway $pCO_2$ measurements (approximately 2% relative uncertainty; Burgers et al., 2017).

## 3 Results and Discussion

### 3.1 Source water mass characteristics and origins

Vertical section plots of tracer concentrations along the Nares Strait transect are shown in Figure 2 (refer to Figure 1a for the transect location). Additionally, Figure 3 displays salinity-property plots for all tracers and stations employed in the eOMP analysis, with source water mass definitions shown as large symbols.

In the northern source region in (Kennedy Channel; blue stations in Figure 1a) we identify three source water masses entering the study region (Figure 3). The shallowest of these water masses is characterized by a sub-surface temperature minimum near the freezing point (-1.7 °C) located at 50 m depth, coinciding with a maximum in $f$CDOM. We refer to this as Polar Mode Water (PMW), as it represents a winter mode water formed by repeated convection from cooling and brine release. PMW is also commonly referred to as the polar mixed layer in the literature of the Amerasian basin of the Arctic Ocean (Peralta-Ferriz & Woodgate, 2015; Rudels et al., 2004). In summer, PMW is altered due to the addition of freshwater from SIM or RR which re-stratifies the surface waters, forming a shallower and warmer surface mixed layer (SML) which is underlain by the temperature minimum of the previous winter's PMW. We observe this transformation beginning to occur downstream in Kane Basin (Figure 2a). We defined the characteristics of PMW by averaging all tracer measurements at the temperature minimum of each station in the northern source region. Our defined properties of PMW overlap in salinity, temperature, and depth with previously described East Siberian cold shelf water (Wang et al., 2021), with the high $f$CDOM observed in this layer also pointing to its origins on the Siberian shelves, where significant inputs of river runoff and extensive seasonal sea-ice formation in winter contribute to the near-freezing temperature and high $f$CDOM (Bauch et al., 2011; Stedmon et al., 2021). The average ANP value of PMW is 0.46, signalling that this layer represents a mixture of Atlantic and Pacific-origin surface waters. The East Siberian Sea is a location where Atlantic and Pacific waters meet, from the easterly coastal flow in the Laptev Sea and the westerly flow of Pacific waters from the Chukchi Sea (Alkire et al., 2021; Semiletov et al., 2005). Further, the Siberian shelves are the source region for waters feeding the Transpolar Drift stream (Charette et al., 2020), which transports them across the Arctic basins towards northern Greenland, and from there into either Nares Strait or Fram Strait. PMW with a strong riverine signal has previously been documented exiting the Arctic region via Fram Strait (Dodd et al., 2012; Gonçalves-Araujo et al., 2016; Granskog et al., 2012), but to our knowledge this

dataset provides the first observational evidence of its passage through Nares Strait.

Below the PMW, a second water mass at intermediate depths (centered around 100 m, about 60 m thick) is characterized by a maximum in dissolved nutrients (e.g., Si, P, DIC; Figure 3). This water mass was defined by fitting a smoothing spline curve through the salinity-silicate measurements of the northern source region (blue stations and data points in Figure 3) and extracting the peak silicate concentration of this curve (17.4 µmol $kg^{-1}$) and its associated salinity (S = 33.2). For all other tracers we similarly fit a smoothing spline curve through the salinity-tracer relationship of the northern source region and extracted the tracer value corresponding to S = 33.2. We identify this source water mass as Upper Halocline Water (UHW), sometimes also referred to as Pacific Winter Water in the literature (Brown et al., 2016; Steele et al., 2004). We find our peak silicate concentration of UHW to be low compared to previous reports of UHW in the Canada Basin, where the silicate maximum has been observed to range from 35 to 45 µmol $kg^{-1}$ (Alkire et al., 2021; Jones & Anderson, 1986; McLaughlin et al., 1996). The average ANP value of UHW in Kennedy Channel is 0.5 (Figure 2c), suggesting that this water mass also represents a mixture of Pacific-source water with Atlantic contributions from the Siberian shelves. Indeed, the NO parameter indicates this as well, displaying relatively low values (368 to 375 µmol $kg^{-1}$; Figure 2d) compared to those typically associated with UHW in the Chukchi Sea and Canada Basin (420 to 430 µmol $kg^{-1}$ and S = 33.1; Alkire et al., 2021). Recent studies have documented waters in the East Siberian Sea that could ventilate the UHW of the deep Arctic basins, and are similarly characterized by a silicate maximum and denitrification signal (Anderson et al., 2013, 2017; Nishino et al., 2013; Wang et al., 2021), but can be distinguished by a decrease in the NO parameter (Alkire et al., 2021). We hypothesize that the UHW observed in Kennedy Channel was likely transported beneath the TPD from the East Siberian Sea across the Makarov Basin towards Nares Strait, roughly aligned with the Pacific-Atlantic front through the central Arctic Ocean.

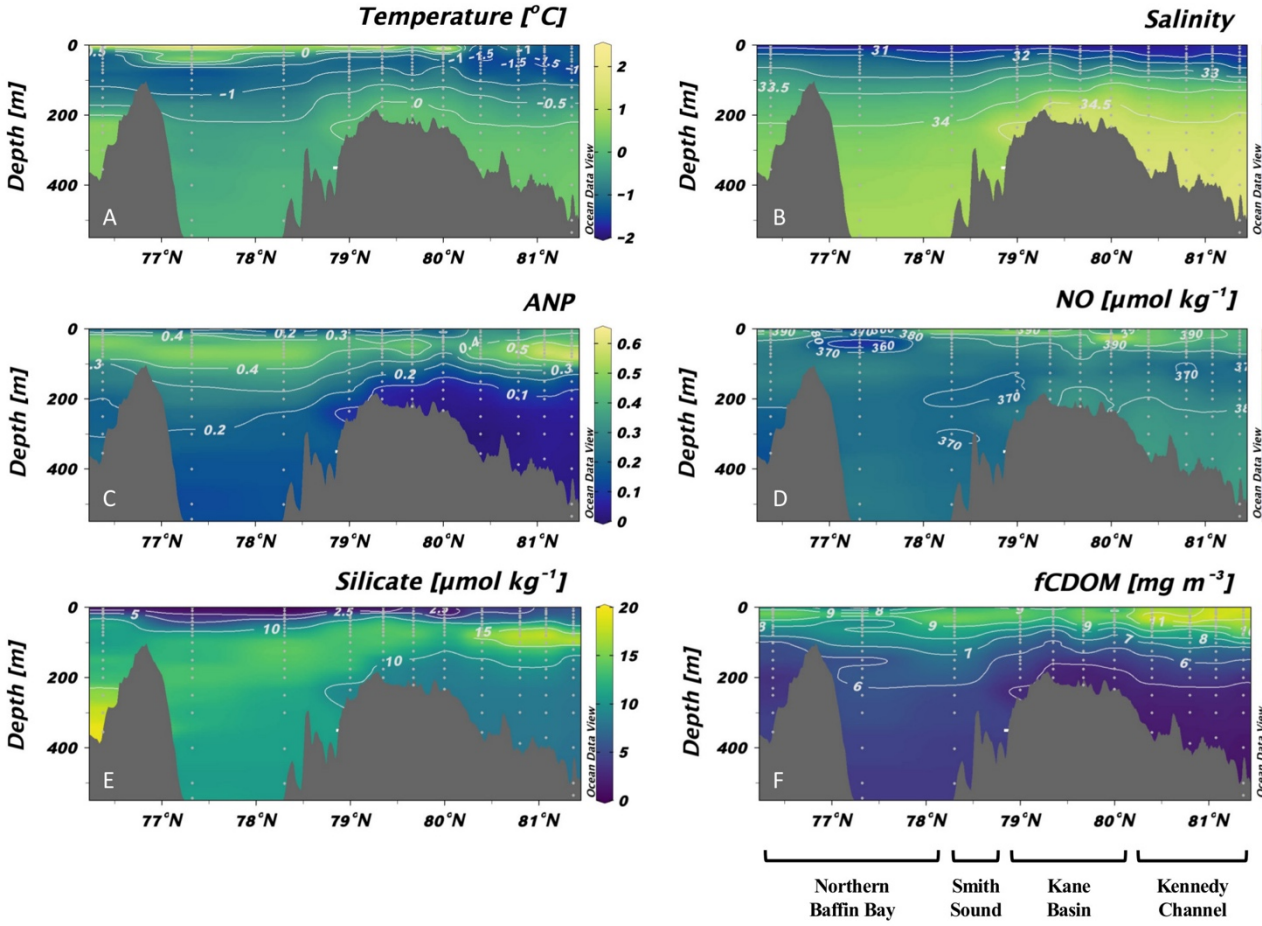


Figure 2: Section plots of (a) temperature, (b) salinity, the (c) ANP, and (d) NO parameters (section 2.3), (e) silicate, and (f) CDOM fluorescence (fCDOM) in Nares Strait (see section outline plotted in red in Figure 1a). Approximate locations of Kennedy Channel, Kane Basin, Smith Sound, and northern Baffin Bay are shown below panel f. Figure created using Ocean Data View software (Schlitzer, 2020).

The deepest water mass entering Nares Strait from the north is characterized by temperatures above 0°C at depths below 200 m, with a maximum temperature of 0.36 °C observed at 500 m depth in Kennedy Channel. This is identified as Canada Basin Atlantic Water (CBAW), as the observed temperature maximum does not exceed 0.5 °C, compared to the warmer temperature maxima of Atlantic water observed in the Amundsen ( 1 °C) and Nansen ( 1.5 – 2 °C) basins (Rudels, 2009).

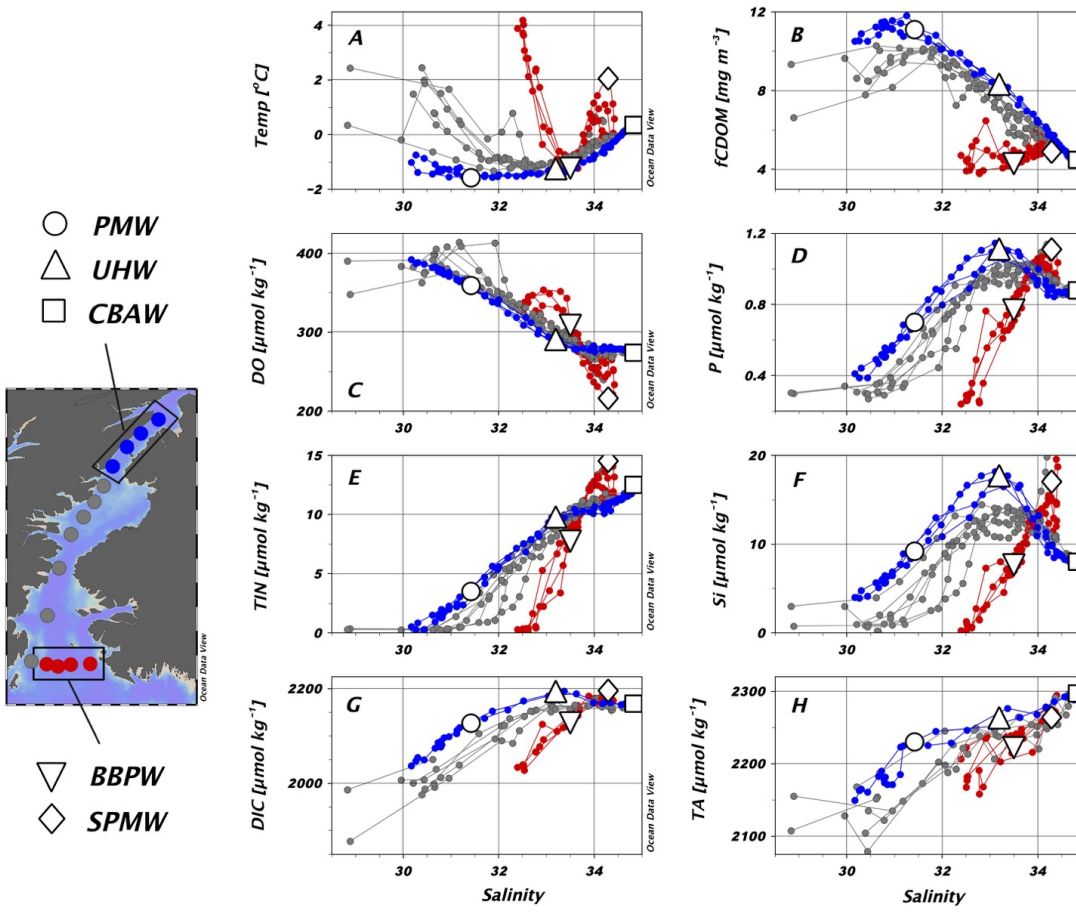


Figure 3: Salinity versus (a) temperature, (b) CDOM fluorescence, (c) dissolved oxygen, (d) phosphate, (e) total inorganic nitrogen (TIN = $NO_3^-$ + $NO_2^-$, + $NH_4^+$), (f) silicate, (g) dissolved inorganic carbon, and (h) total alkalinity for all stations in Nares Strait and the NOW polynya region of northern Baffin Bay. Data from stations designated as the northern source region are plotted in blue in each panel, stations designated as the southern source region are plotted in red, with stations in between the two source regions plotted in grey. Source water mass definitions are plotted as open symbols: circle, polar mode water (PMW); upward triangle, upper halocline water (UHW); square, Canada Basin Atlantic water (CBAW); inverted triangle, Baffin Bay Polar Water (BBPW); diamond, sub-polar mode water (SPMW). Tracer measurements from the northern source region were used to define properties of the PMW, UHW, and CBAW, whereas measurements from the southern source region were used to define BBPW and SPMW properties (see text in section 3.1 for details). Figure created using Ocean Data View software (Schlitzer, 2020).

From the southern source region (red stations in Figure 1a) we identify two more source water masses entering the study region. The uppermost water mass is characterized by a temperature minimum that is observed as a characteristic "knee" in the *TS* diagram (Figure 3a). This is identified as Baffin Bay Polar Water (BBPW; Mortensen et al., 2022; Rysgaard et al., 2020), a winter mode water previously documented along the West Greenland continental slope from Disko Bay to the NOW region (Bâcle et al., 2002; Lobb et al., 2003; Myers et al., 2009; Rysgaard et al., 2020; Tang et al., 2004). The exact formation site of BBPW currently remains unknown (Mortensen et al., 2022). In the literature BBPW is characterized by a temperature minimum near the freezing point (around -1.8 °C) and salinity of 33.6 (Rysgaard et al., 2020). The BBPW we observe in the southeastern NOW is characterized by an average temperature minimum of -1.15 °C and a salinity of 33.5, suggesting it has been somewhat diluted from its original characteristics at its point of origin. Our defined BBPW properties were calculated by averaging all tracer measurements at the temperature minimum of each station in the southern source region.

A second relatively deep and warm water mass is observed entering the southern source region at 300 m depth. This water mass is characterized by a temperature maximum of 2 °C at a salinity of 34.3, as well as a pronounced DO minimum and maximum in nutrient concentrations of TIN, P, Si, and DIC (Figure 3). We identify this as Subpolar Mode Water (SPMW), which originates in the subpolar North Atlantic as a winter mode water before being transported around Cape Farewell by the Irminger Current and continuing northwards into Baffin Bay with the WGC (Rysgaard et al., 2020). This water mass has also formerly been referred to in the literature as Irminger Water, West Greenland Irminger Water, or winter Atlantic water (Azetsu-Scott et al., 2012; Curry et al., 2014; Myers et al., 2009; Randelhoff et al., 2019). Our definition of SPMW (Table 1) represents the properties observed at the deep temperature maximum at station 115. Rysgaard et al. (2020) distinguish between upper and deep SPMW in their classification of water masses over the West Greenland shelf and slope. Our observations represent a modified version of their deep SPMW (i.e., T = 4 °C, S = 34.7), due to cooling and mixing with relatively fresh water masses as it progresses northwards (Rysgaard et al., 2020). The high nutrient and low DO concentrations of SPMW are likely the result of strong remineralization of organic matter, exported to depth from the highly productive surface waters of the West Greenland shelf in southeastern Baffin Bay (Burgers et al., 2020).

Many previous investigations of water mass properties in northern Baffin Bay have relied solely on temperature and salinity measurements. Our additional geochemical tracers reveal that the water mass assembly from our southern source region (influenced by the WGC) can be distinguished from the northern water mass assembly (Arctic outflow waters) by very different salinity-tracer relationships (Figure 3).

### 3.2 Modeled source water mass distributions

Figure 4 shows vertical sections of the eOMP-calculated mixing fractions of

source water masses along the Nares Strait transect. From north to south in Nares Strait the water mass assembly transitions from being dominated by PMW, UHW, and CBAW in Kennedy Channel, to being significantly influenced by intrusions of BBPW and SPMW in northern Baffin Bay. Within the upper 50 m we observe a slow north-to-south dilution of the PMW layer due to increasing fractions of RR (2 to 9%) and SIM (2 to 7%), as well as intrusions of BBPW (20 – 60%) south of Smith Sound. At station 120 (77.3 °N) an intrusion of BBPW at 40 m depth is also associated with fractions of SIM up to 5%. This intrusion likely represents surface waters from the WGC interleaving with Arctic outflow waters at the appropriate density horizon.

Below the upper 50 m of the Nares Strait transect, fractions of UHW and CBAW also undergo a similar north-to-south dilution due to northward intrusions of BBPW and SPMW. The complex bathymetry in the region also plays an important role in directing this interaction. As Arctic-sourced UHW and CBAW enter Kane Basin they encounter a rapidly shoaling bathymetry, leading to slight upwelling of these layers. In the surface waters (upper 20 m) of Kane Basin some UHW fractions between 30 – 60% are observed, possibly due to upwelling and some upward mixing by strong tidal motions (Münchow, 2016). We speculate that these surface UHW fractions may be overestimated, as they are not supported by a matching increase in nutrient concentrations (e.g., Si, DIC, TIN) at the surface (see Figure 2). Within Kane Basin maximum fractions of UHW decreased to approximately 50%, being mixed with BBPW fractions up to 45%. A pulse of SPMW with fractions up to 15% also interleaves between layers of UHW and CBAW at approximately 120 m depth in Kane Basin. South of the Kane Basin sill, the remaining UHW and CBAW layers sink down to greater depths, with CBAW fractions dominating the water column below 200 m. At station 127 (78.3 °N) we observe UHW fractions between 20 –

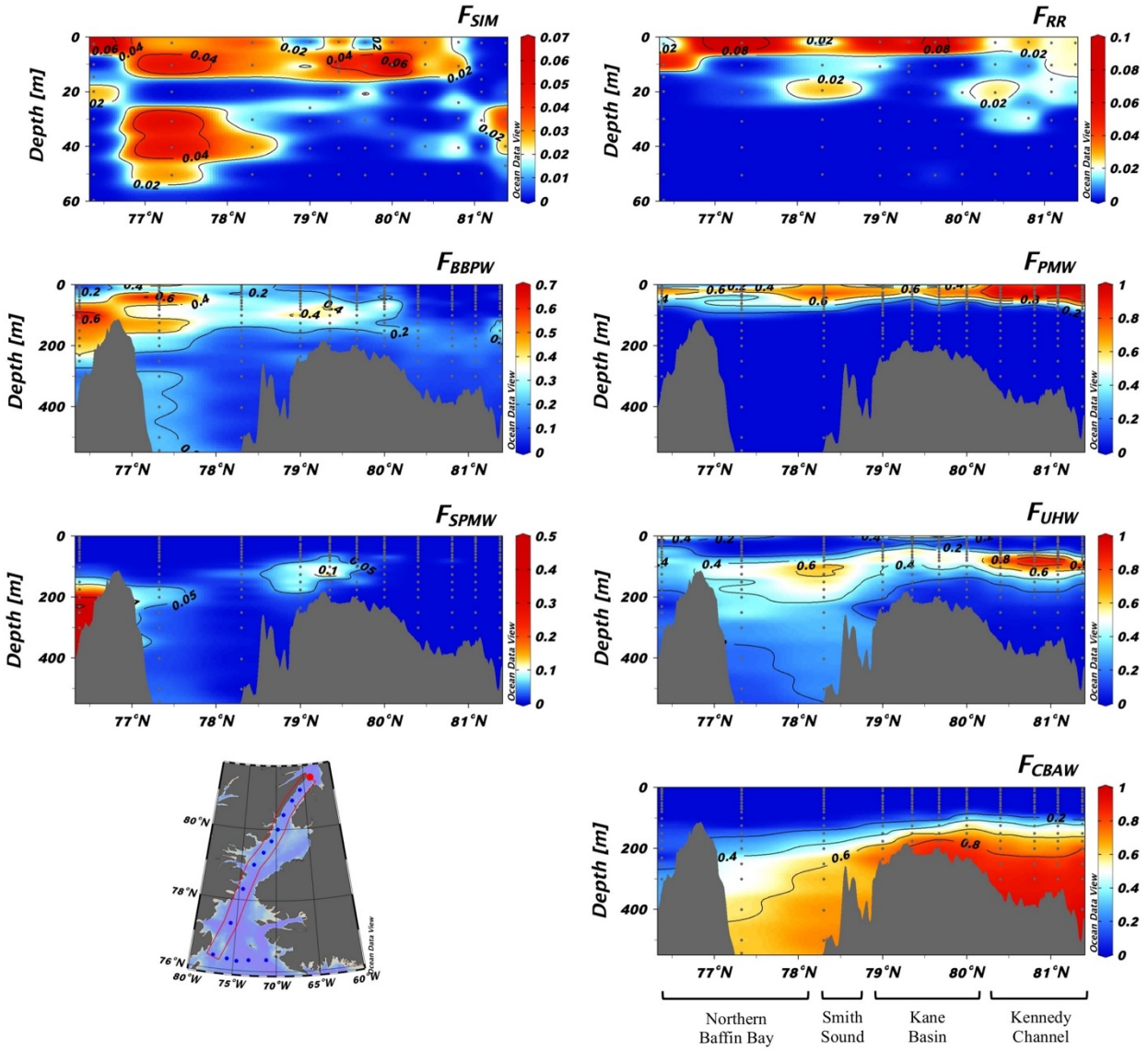


Figure 4: Calculated source water mass fractions along the Nares Strait transect (transect location shown in bottom left map). Freshwater sources are sea-ice melt (SIM) and river runoff (RR), note the depth scale is reduced to the upper 60 m for freshwater panels. Source water masses are: Baffin Bay Polar water (BBPW), Subpolar Mode water (SPMW), Polar Mode water (PMW), Upper Halocline water (UHW), and Canada Basin Atlantic water (CBAW). Note the different colour scales on all panels. Figure was created using Ocean Data View software (Schlitzer, 2020).

30% mixed into the CBAW layer below 200 m. At station 120 (77.3 °N) fractions of BBPW (less than 20%) are mixed with CBAW below 300 m. Station 101 (at the southern end of the Nares Strait transect) is located at the site of a large hollow in the seafloor, isolated on all sides by banks of 100 – 200 m in depth. Here we find the water column below 200 m to contain SPMW fractions (up to 56%), mixed with 20 to 40% BBPW above 300 m, and 20 to 25% CBAW below 300 m. The upper water column at station 101 contains mostly PMW (up to 75%) at depths above 60 m, with a mixture of BBPW (40 to 65%) and UHW (25 to 45%) between 60 m and 200 m depth.

Figure 5 displays vertical sections of mixing fractions across the east-west NOW transect in northern Baffin Bay. At station 115 (easternmost station of the transect) the surface mixed layer is composed of mainly BBPW fractions (above 90%) with fractions of SIM from 7 to 9%. This surface layer spreads from east to west across the NOW region, retaining BBPW fractions above 80% and low SIM fractions (above 2%) until reaching station 101 in the east where the PMW from the Arctic dominates the surface waters associated with RR fractions between 2 and 5%. Also at station 115 in the east we can see the entrance of SPMW into the region at 300 m depth. Since low fractions of SPMW are seen at station 111 (immediately west of station 115), we assume SPMW transits northwards from station 115 following a deep ($>$ 400 m) trough around the east side of the Carey Islands (Figure 1a). This flow path might also explain why our eOMP fractions do not indicate significant SPMW fractions at stations 120 and 127 in northern Baffin Bay, but do show small fractions (up to 15%) arriving in Kane Basin (Figure 4). It is possible that our sampling stations 120 and 127 were located west of the northward moving SPMW fractions. Results at station 111 indicate that the western side of the deep trough through the NOW region plays an important role transporting a mixture of UHW and CBAW southwards into northern Baffin Bay at depths below 150 m. At stations 108, 105, and 101 (west of 74 °W) we observe the southward return of SPMW from its northern detour to Kane Basin. At all stations across the NOW transect we observe a mixture of mostly CBAW (50 – 60%) and some UHW (20 – 30%) flowing southwards below the layer dominated by SPMW. These results fit well with previous observations by Lobb et al. (2003) of "a near-bottom intrusion of relatively cold water" within the WGC-dominated area of warm SPMW in the eastern NOW region. Our water mass distributions also match the results of Melling et al. (2001) who documented the cyclonic flow of warm SPMW throughout the NOW region, noting that SPMW "transits northwards following the eastern edge of a deep channel that is 600 m in depth extending northward as far as Smith Sound" before joining with the Arctic outflow flowing southwards out of Nares Strait.

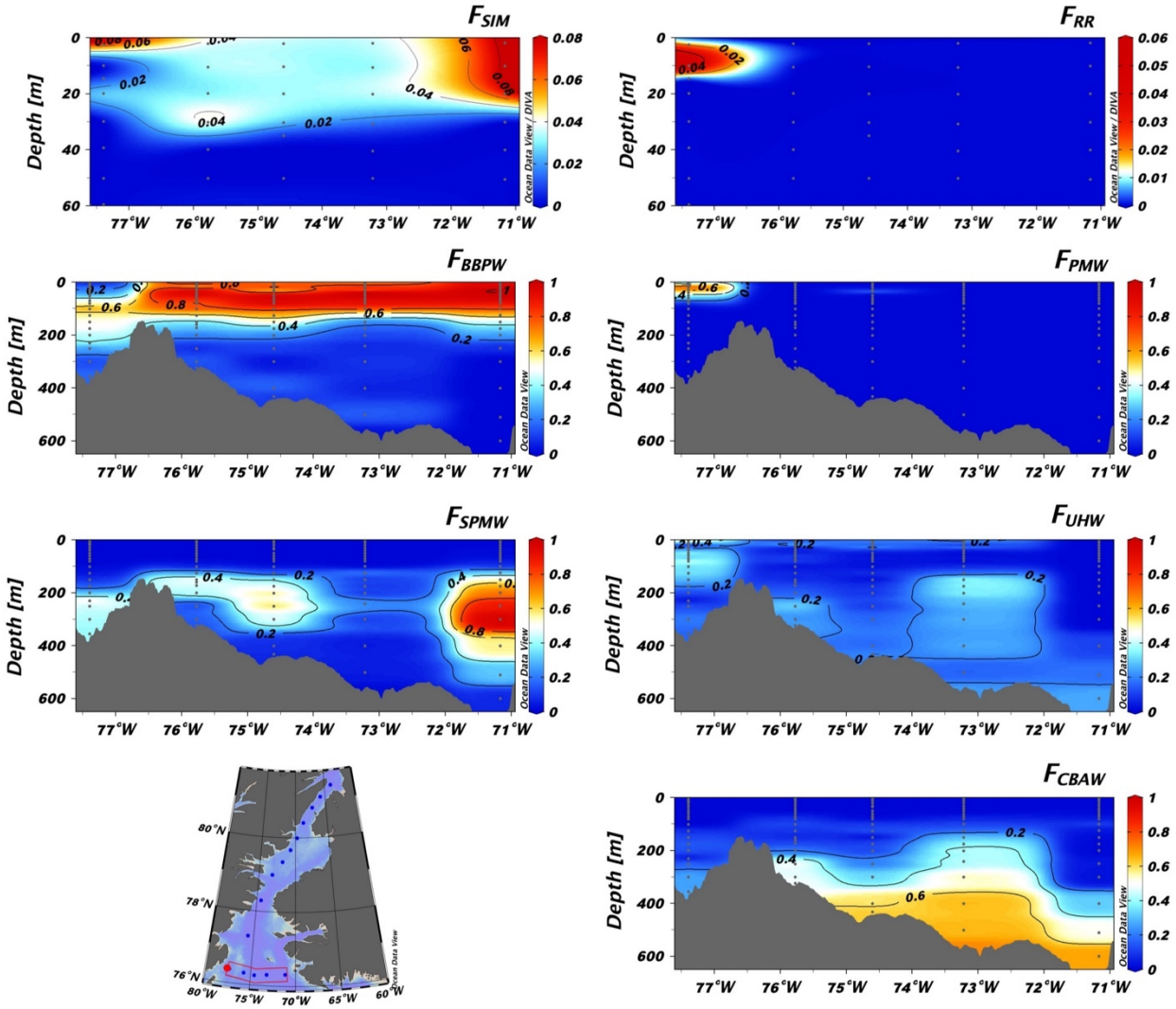


Figure 5: Calculated source water mass fractions across the NOW transect (transect location shown in bottom left map). Freshwater sources and source water masses are the same as shown in Figure 4. Note the different colour scales and shorter depth scale of the top two freshwater panels. Figure was created using Ocean Data View software (Schlitzer, 2020).

### 3.3 Carbonate system

Figure 6 shows section plots of the $CO_2$ system variables DIC, TA, $pCO_2$, $pH_T$, $\Omega_{Ar}$, and $\Omega_{Ca}$ along the Nares Strait transect. Both DIC and TA display considerable variability throughout Nares Strait, with surface concentrations decreasing by roughly 200 µmol kg$^{-1}$ and 100 µmol kg$^{-1}$, respectively, from north to

south. Increasing freshwater inputs and biological DIC drawdown by a moderate phytoplankton bloom in Kane Basin drive these decreases (biological impacts will be further discussed in section 3.4). In Kennedy Channel, there is a slight DIC maximum located at a depth of 100 m, coinciding with the silicate maximum of the UHW (see Figures 2e and 3f). However, the peak DIC concentration observed in this layer (2194 µmol $kg^{-1}$ at station Ken1) is not as high as DIC concentrations that have been observed in the UHW of the Canada Basin (2225 to 2260 µmol $kg^{-1}$; Brown et al., 2016; Miller et al., 2014). The UHW in Kennedy Channel also displays a maximum in $pCO_2$ (490 ± 20 µatm), and minima in $pH_T$, $\Omega_{Ar}$, and $\Omega_{Ca}$ (7.95 ± 0.03, 1.00 ± 0.05, and 1.60 ± 0.09, respectively). Below the UHW layer in Kennedy Channel there is a modest decrease in DIC with depth, indicating transition to CBAW. CBAW also displays relatively lower $pCO_2$ (350 ± 10 µatm) and relatively higher $pH_T$ (8.05 ± 0.03), $\Omega_{Ar}$ (1.30 ± 0.07), and $\Omega_{Ca}$ (2.10 ± 0.12), compared to the UHW layer above.

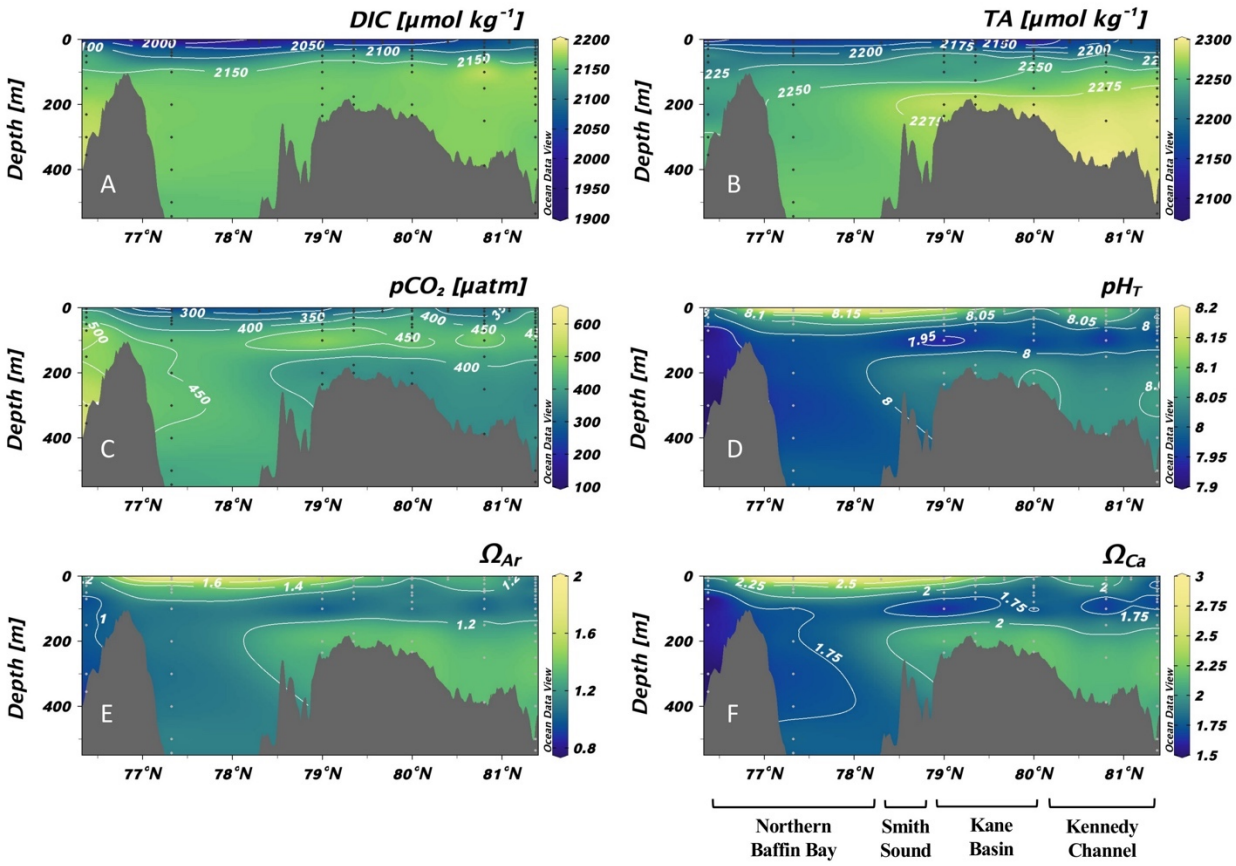


Figure 6: Section plots of carbonate chemistry measurements along the Nares Strait transect (transect outline shown in red in Figure 1a). Figure created

using Ocean Data View software (Schlitzer, 2020).

In Kane Basin the subsurface DIC maximum that was observed in Kennedy Channel is eroded. At the same time TA concentrations in the intermediate water column decrease between depths of 80 and 150 m, with salinities between 33.5 and 34.4. This coincides with the locations and salinities of BBPW and SPMW intrusions in Kane Basin (Figure 4). Both BBPW and SPMW are characterized by lower TA in comparison to UHW and CBAW of the northern water mass assembly (Table 1). The TA decrease observed in Kane Basin compensates for the erosion of the UHW DIC-maximum in maintaining a high $pCO_2$ and low pH and $\Omega$ layer throughout Kane Basin.

South of Kane Basin (at station 120; Figure 1a) we also note a TA decrease at depths greater than 200 m, compared to conditions farther north (Figure 6b). This represents the dilution of CBAW by mixing with UHW and intrusions of BBPW and SPMW (Figure 4), all of which are characterized by lower TA concentrations compared to CBAW (Table 1). This TA decrease at depth also leads to a relative decrease in $pH_T$, $\Omega_{Ar}$, and $\Omega_{Ca}$, and a relative increase in $pCO_2$ in the deep waters of the northern NOW region. The lowest observations of $pH_T$, $\Omega_{Ar}$, and $\Omega_{Ca}$, (and highest $pCO_2$) throughout the Nares Strait transect were observed below 100 m at the southern end of the transect at station 101, coinciding with relatively high fractions of SPMW filling a deep hollow, and high BBPW fractions (up to 65%) sitting above (Figure 4).

Figure 7 displays vertical section plots of the same the carbonate system variables across the NOW transect. Here we can see that SPMW entering the study region at the eastern end of the transect (station 115 at 300 m depth) is characterized by low $pH_T$ (7.9 $\pm$ 0.4), low $\Omega_{Ar}$ (0.94 $\pm$ 0.05), and high $pCO_2$ (610 $\pm$ 20 µatm). In fact, high SPMW fractions ($>$ 40%) across the NOW transect (Figure 5) show the lowest observed $pH_T$, $\Omega_{Ar}$ and $\Omega_{Ca}$ throughout the study region. Other characteristics of SPMW, such as high nutrient concentrations (Figure 3) and high AOU (Figure S5) indicate that this water mass likely transports a strong remineralization signal due to the export of organic material from the productive West Greenland shelf (Burgers et al., 2020). It is interesting to note that the lowest $pH_T$ observation (7.8 $\pm$ 0.5) was observed at 150 m depth at station 108 in the middle of the transect (Figure 1a), at the boundary between the BBPW and SPMW layers. This minimum value is possibly due to a questionably low TA measurement at this location as it cannot be explained by obvious chemical or biological processes (see Figure 7b). BBPW entering the region at station 115 (Figure 5) also displayed relatively low $pH_T$ (8.0 $\pm$ 0.3), $\Omega_{Ar}$ near saturation (1.09 $\pm$ 0.06), and relatively high $pCO_2$ (440 $\pm$ 20). The upper 80 m of the central three stations (105, 108, and 111) of the NOW transect displayed lower $pCO_2$ (below 350 µatm), and higher $pH_T$ ($>$ 8.05) and $\Omega_{Ar}$ ($>$ 1.4) due to the impact of a surface bloom (Figure S5) and inputs of SIM (Figure 5).

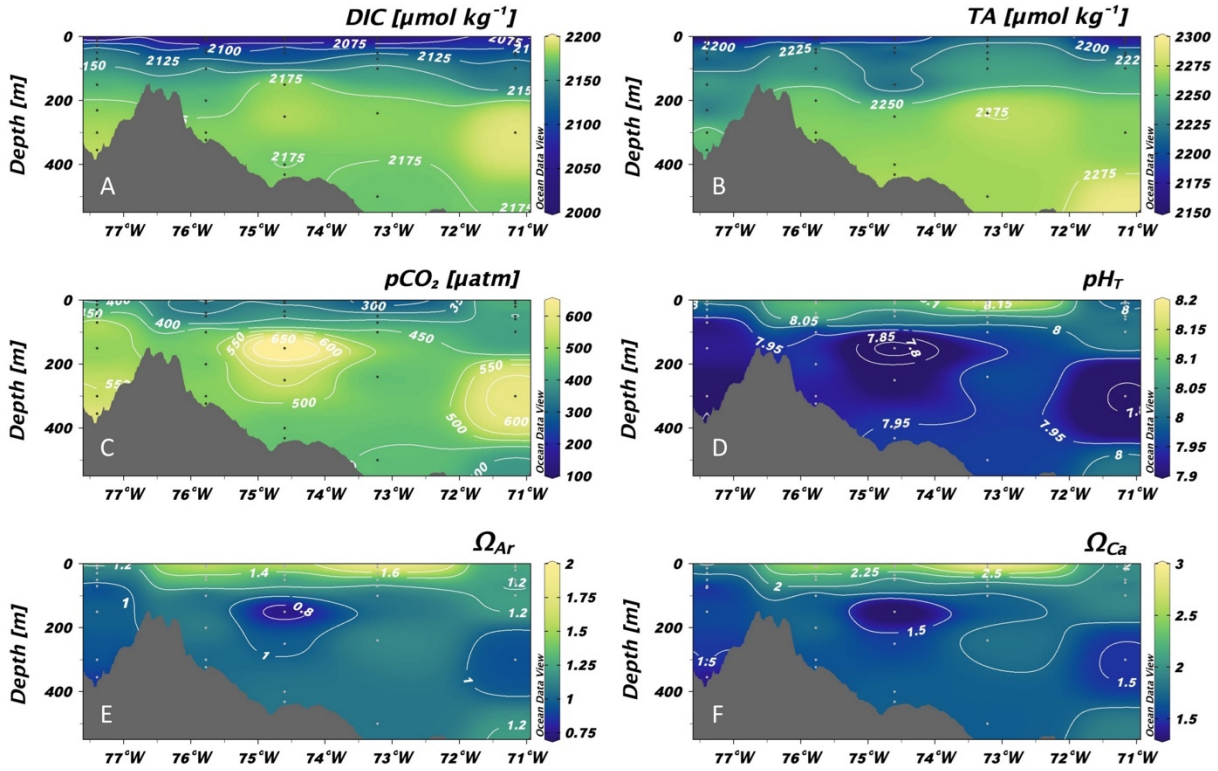


Figure 7: Section plots of carbonate chemistry measurements across the NOW transect (transect outline shown in inset map of Figure 5). Figure created using Ocean Data View software (Schlitzer, 2020).

### 3.4 Biological concentration changes ($\Delta DIC_{bio}$)

The $\Delta DIC_{bio}$ term (Equation 4) estimates the cumulative change in DIC concentrations due to *in-situ* biological activity (photosynthesis, respiration) relative to the concentration that would be expected due solely to water mass mixing ($DIC_{mix}$) within the eOMP framework. Positive values of $\Delta DIC_{bio}$ indicate DIC addition due to net respiration, while negative values represent DIC removal due to net photosynthesis. Figure 8 shows section plots of $\Delta DIC_{bio}$, AOU, chlorophyll-*a* fluorescence, and TIN concentrations throughout the upper 100 m of the Nares Strait transect. We observe a clear divide between the surface and deeper waters, with negative values of $\Delta DIC_{bio}$ extending from the surface to depths of 40 m, and mostly near-zero (or slightly positive) values of $\Delta DIC_{bio}$ in deeper waters.

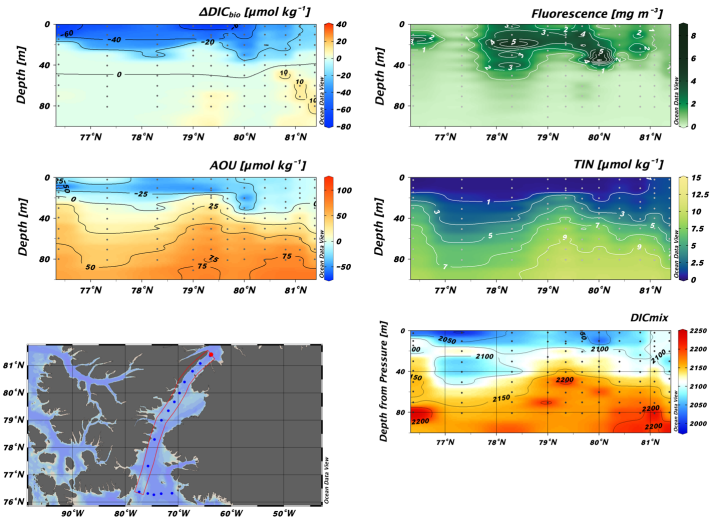


Figure 8: Section plots of biologically driven changes in DIC ($\Delta DIC_{bio}$), chlorophyll-a fluorescence, Apparent Oxygen Utilization (AOU), and total inorganic nitrogen (TIN) throughout the upper 100m of the Nares Strait transect (same transect as Figures 2, 4, and 6). Figure was created using Ocean Data View software (Schlitzer, 2020).

Within the upper 40 m of the Nares Strait transect negative values of $\Delta DIC_{bio}$ indicate a modest phytoplankton bloom, which progresses through multiple phases as waters transit southwards from Kennedy Channel. Section plots of chlorophyll-*a* fluorescence and total inorganic nitrogen (TIN) concentrations in Figure 8 illustrate the different bloom stages and nutrient limitations that drive them. The initial surface bloom in Kennedy Channel is weak, owing to the low initial concentrations of TIN available in the surface mixed layer (less than 2 µmol $kg^{-1}$). Due to the nutrient depleted surface waters, a subsurface chlorophyll maximum (SCM) develops at the entrance to Kane Basin (around 80 °N) at 35 m depth. Further into Kane Basin the shallowing bathymetry approaching 79 °N injects some UHW fractions and nutrients into the surface mixed layer (Figure 4). This addition of nutrients spurred a second bloom in Kane Basin, which is associated with the strongest $\Delta DIC_{bio}$ drawdown of -73 µmol $kg^{-1}$ at the surface (at approximately 79.5 °N). In Smith Sound (around 78.5 °N) the bloom is still well developed but the SCM extends deeper owing to nutrient drawdown at the surface. Here surface values of $\Delta DIC_{bio}$ slightly increase (decreasing photosynthesis) to around -50 µmol $kg^{-1}$. By the time surface waters exit Smith Sound into northern Baffin Bay (around 77.3 °N) the fluorescence signal had decreased and $\Delta DIC_{bio}$, which integrates the effects of upstream processes, remained approximately the same as in Smith Sound. This sudden cessation of any fluorescence signal may be associated with the northward intrusion of surface waters from the WGC (a mixture of BBPW and SIM mostly; Figure 4) containing low nutrient concentrations (Table 1). We also suggest that

enhanced air-sea gas exchange may have contributed to the increase in AOU and slight decrease in $\Delta DIC_{bio}$ (see section 3.5), and the apparent increase in AOU toward equilibrium with the atmosphere. Finally, at the southernmost station of the Nares Strait transect an SCM is observed at 15 m depth, with surface $\Delta DIC_{bio}$ decreasing slightly again to -66 µmol $kg^{-1}$ (indicating increasing primary production) and AOU decreasing slightly as well.

We do not observe any significant net respiration signal (positive $\Delta DIC_{bio}$) in Nares Strait (see Figure S6 for a full vertical section of $\Delta DIC_{bio}$ along the Nares Strait transect). Within Kennedy Channel there are some low positive $\Delta DIC_{bio}$ values ranging from 3 to 12 µmol $kg^{-1}$, coinciding with the location of the UHW layer in the water column (Figure 8). However, these positive $\Delta DIC_{bio}$ estimates are approximately equal to the residual DIC term from the eOMP output (8 µmol $kg^{-1}$; Table 2), indicating that these small net respiration estimates may simply be the result of uncertainty within the eOMP framework. In Kennedy Channel, it is likely manifested by some natural variability in the observed peak nutrient concentrations at each station. These results suggest that net respiration within the water column of Nares Strait is likely negligible. Only at the southernmost station of the transect (station 101), in the relatively isolated hollow dominated by SMPW (Figure 4) do we find a significant signal of net respiration (Figure S6).

Across the east-west transect in the NOW region we do observe positive $\Delta DIC_{bio}$ values ($>$ 20 µmol $kg^{-1}$) at depths below 300 m (see Figure S5). The greatest positive $\Delta DIC_{bio}$ value of 32 µmol $kg^{-1}$ was located in the deep hollow at station 101. We hypothesize that this results in part from the confined nature of the water in the hollow, as well as remineralization of any exported organic material that ends up in this isolated deep water. Positive $\Delta DIC_{bio}$ values up to 29 µmol $kg^{-1}$ are also observed below 300 m depth at station 115, at the eastern end of the transect. We presume this is due to remineralization of organic material transported with the waters of the WGC, seeing as the high $\Delta DIC_{bio}$ values do not extend deeper (below 500 m depth) where significant CBAW fractions were located (Figure 5).

### 3.5 Gas exchange term ($\Delta DIC_{gas}$)

Table 3 shows estimated $\Delta DIC_{gas}$ values at each sampling station of the Nares Strait transect, with positive values indicating that the surface ocean acts as a sink of atmospheric $CO_2$. Due to the consistent undersaturation of surface water $pCO_2$ in Nares Strait, the whole study region was an atmospheric $CO_2$ sink. As expected, $\Delta DIC_{gas}$ estimates start off small in Kennedy Channel, where surface waters had only recently emerged from under the ice arch. $\Delta DIC_{gas}$ estimates slightly increased in Kane Basin, where biological drawdown of DIC and increasing SIM fractions contribute to decreasing surface water $pCO_2$ and surface mixed layer depths. $\Delta DIC_{gas}$ increases substantially in Smith Sound (station 127) and northern Baffin Bay (station 120 and 101), where wind speeds increased significantly (see Figure 5 of Burgers et al., 2017), and surface mixed layer depths remained shallow. At station 127 the $\Delta DIC_{gas}$ term becomes comparable to

the maximum $\Delta DIC_{bio}$ drawdown in Kane Basin (Figure 8). Further south at station 120 the $\Delta DIC_{gas}$ term has surpassed the maximum $\Delta DIC_{bio}$ drawdown. This is possibly also represented in our surface underway $pCO_2$ measurements, which increase south of station 127 (south of 78.3 °N, Figure 9a). The largest spike in underway $pCO_2$ around latitude 77.5 °N coincides with the highest wind speed observations in this region, suggesting that enhanced air-sea gas exchange may be responsible. This is also likely the reason why we observe an increase in AOU in the surface mixed layer at station 120 in northern Baffin Bay (section 3.4; Figure 8), as gas exchange would have also led to uptake of atmospheric $O_2$.

Table 3: Summary of surface $pCO_2$ measurements (underway and surface rosette bottle) and $\Delta DIC_{gas}$ estimates within the surface mixed layer (SML) at each station of the Nares Strait transect.

| | | | Underway | Surface Bottle | $pCO_2$ difference | Days since | |
|---|---|---|---|---|---|---|---|
| Station | Latitude (°N) | SML (m) | $pCO_2$ (µatm) | $pCO_2$ (µatm) | (Underway - Bottle) (µatm) | ice arch | $\Delta DIC_{gas}$ (µmol kg$^{-1}$) |
| Ken1 | 81.37 | 9.9 | 357.3 | 347.1 | 10.2 | 0.4 | 0.1± 0.0 |
| Ken2 | 81.08 | 18.8 | 351.1 | 354.4 | -3.2 | 2.1 | 1.4 ± 0.4 |
| Ken3 | 80.80 | 14.8 | 312.1 | 320.9 | -8.8 | 3.7 | 3.5 ± 0.9 |
| Ken4 | 80.40 | 7.9 | 302.0 | 314.6 | -12.7 | 5.8 | 6.5 ± 1.5 |
| Kane1 | 80.00 | 8.9 | 295.6 | 299.4 | -3.8 | 7.6 | 8.0 ± 1.8 |
| Kane2 | 79.67 | 11.9 | 298.5 | 293.9 | 4.6 | 9.4 | 16.3 ± 3.5 |
| Kane3 | 79.35 | 10.9 | 264.7 | 278.3 | -13.6 | 11.0 | 20.1 ± 4.2 |
| Kane5 | 79.00 | 10.9 | 251.0 | 243.0 | 8.0 | 12.7 | 18.7 ± 4.0 |
| 127 | 78.30 | 9.9 | 248.6 | 255.8 | -7.2 | 16.0 | 53.3 ± 11.7 |
| 120 | 77.32 | 3.0 | 270.3 | 125.7 | 144.6 | 20.4 | 131.6 ± 27.5 |
| 101 | 76.38 | 7.9 | 273.6 | 318.3 | -44.7 | 24.3 | 186.9 ± 38.4 |

### 3.6 DIC budget in Nares Strait

Table 4 presents average values of $DIC_{mix}$, $\Delta DIC_{bio}$, and $\Delta DIC_{gas}$ in three sub-regions of Nares Strait: (1) Kennedy Channel, (2) Kane Basin, and (3) northern Baffin Bay. The northern Baffin Bay region includes stations 127, 120 and 101 (Figure 1a). The average DIC budget terms are also summarized by depth intervals, between the surface mixed layer (see Table 3 for depths), intermediate depths (50 – 150 m) and the deep water column (> 200 m).

Table 4: Regionally averaged $DIC_{mix}$ (Eq. 3), $\Delta DIC_{bio}$ (Eq. 4), and $\Delta DIC_{gas}$ (Eq. 5) in the surface mixed, intermediate (50 – 100 m), and deep (> 150 m) layers of Kennedy Channel, Kane Basin, and northern Baffin Bay (including Smith Sound) sub-regions of Nares Strait. All DIC budget values are in units of µmol kg$^{-1}$. Insignificant values are not included.

| | Kennedy Channel | Kane Basin | Northern Baffin Bay |
|---|---|---|---|
| | Surface mixed layer | | |
| $DIC_{mix}$ | 2086 ± 20 | 2057 ± 17 | 2040 ± 31 |
| $\Delta DIC_{bio}$ | -23 ± 6 | -54 ± 14 | -56 ± 10 |
| $\Delta DIC_{gas}$ | 3 ± 3 | 16 ± 5 | 123 ± 26 |
| | Intermediate (50 - 150 m) | | |
| $DIC_{mix}$ | 2184 ± 4 | 2172 ± 4 | 2158 ± 8 |
| $\Delta DIC_{bio}$ | 6 ± 5 | 5 ± 3 | - |
| | Deep (>200 m) | | |
| $DIC_{mix}$ | 2174 ± 5 | 2170 ± 7 | 2172 ± 4 |
| $\Delta DIC_{bio}$ | - | - | 8 ± 9 |

Predictably, we find that water mass mixing and transport (captured by the $DIC_{mix}$ term) is responsible for most of the DIC variability across the region. Within the surface mixed layer $DIC_{mix}$ estimates decreased from 2105 µmol $kg^{-1}$ at station Ken1 to 2026 µmol $kg^{-1}$ at station 101 in northern Baffin Bay. This decrease partially results from the intrusion of surface waters from the WGC (a mixture of BBPW and SIM), which contain less DIC than the PMW waters exiting the Arctic Ocean, and also partially from increasing freshwater contributions (SIM and RR) in the surface mixed layer of Nares Strait (Figure 4). At intermediate depths we also find a decrease in $DIC_{mix}$ from Kennedy Channel towards northern Baffin Bay. This is due to the interaction of UHW with BBPW (and some small fractions of SPMW) in Kane Basin, and even higher BBPW fractions present at this depth range in northern Baffin Bay (Figure 4). $DIC_{mix}$ concentrations at depths below 200 m remained essentially constant across Kennedy Channel, Kane Basin, and northern Baffin Bay despite changes in source water mass fractions transitioning from mainly CBAW in the north to a mixture of CBAW with UHW and BBPW contributions in northern Baffin Bay.

Despite the fact that $\Delta DIC_{bio}$ represents a relatively small portion of the overall DIC pool, we find it plays an important role in determining surface $pCO_2$ concentrations. We investigated the contributions of water mass mixing and biology to the observed $pCO_2$ of the surface mixed layer $pCO_2$(obs) from surface rosette samples in Nares Strait (blue diamonds in Figure 9a), by comparison with hypothetical values of $pCO_2$(mix) and $pCO_2$(mix+bio) derived from $CO_2$ system calculations in $CO_2$Sys. The term $pCO_2$(mix) represents the surface $pCO_2$ due solely to water mass mixing and was calculated from inputs of average $DIC_{mix}$, $TA_{mix}$, in-situ $S_P$, and in-situ temperature within the surface mixed layer of each station. The term $pCO_2$(mix+bio), representing the surface $pCO_2$ due to water mass mixing and biology, is calculated from inputs of $DIC_{mix}$+ $\Delta DIC_{bio}$, $TA_{mix}$+ $\Delta TA_{bio}$, in-situ $S_P$, and in-situ temperature. Here we factor in a slight increase in TA due to nitrate uptake during primary production, which can be estimated as $\Delta TA_{bio} = (\frac{11}{106})\Delta DIC_{bio} = 6$ µmol $kg^{-1}$, assuming that one unit of nitrate uptake increases TA by one unit, and applying our local Redfield ratios

(11 TIN : 106 DIC).

Figure 9b displays the terms $pCO_2$(mix), $pCO_2$(mix+bio), and $pCO_2$(obs) for the surface mixed layer at each station along the Nares Strait transect. Here we can see that biology plays a major role in lowering surface $pCO_2$ in Nares Strait, especially in Kane Basin where upwelling of UHW fractions increases the $pCO_2$(mix) term. The only station where biology does not fully account for the difference between $pCO_2$(mix) and $pCO_2$(obs) is station 120. The rosette samples at this station indicate a very sharp gradient in surface $pCO_2$ between the surface and 10 m depth (Figure 9a). CTD profiles of temperature and salinity at station 120 also show steep near-surface gradients with salinity decreasing from 31.0 at 10 m to 28.4 at 2 m, and temperature increasing from 1.8 to 2.6 °C (not shown). Such steep gradients likely indicate strong surface freshwater stratification, an occurrence that is known to cause considerable uncertainty in the accurate quantification of surface $pCO_2$, and air-sea $CO_2$ flux estimates in Arctic coastal waters (Ahmed et al., 2020; Dong et al., 2021; Miller et al., 2019). Indeed, our eOMP calculated freshwater fractions indicate relatively high fractions of both RR and SIM in the surface waters at station 120 (Figure 4). However, the $pCO_2$(mix) term at station 120 remains high (approximately 490 µatm) despite these freshwater contributions. We also note an unusually high surface TA measurement at station 120 (at 2 m depth; TA = 2155 µmol $kg^{-1}$), despite very low salinity and DIC measurements at the same location (S = 28; DIC = 1877 µmol $kg^{-1}$). Therefore, it is also possible that a questionable surface TA measurement is responsible for the abnormally low surface $pCO_2$(obs) at station 120. Underway $pCO_2$ measurements at station 120 (270 µatm; Table 3; Figure 9a) are in closer agreement with the $pCO_2$(mix+bio) term.

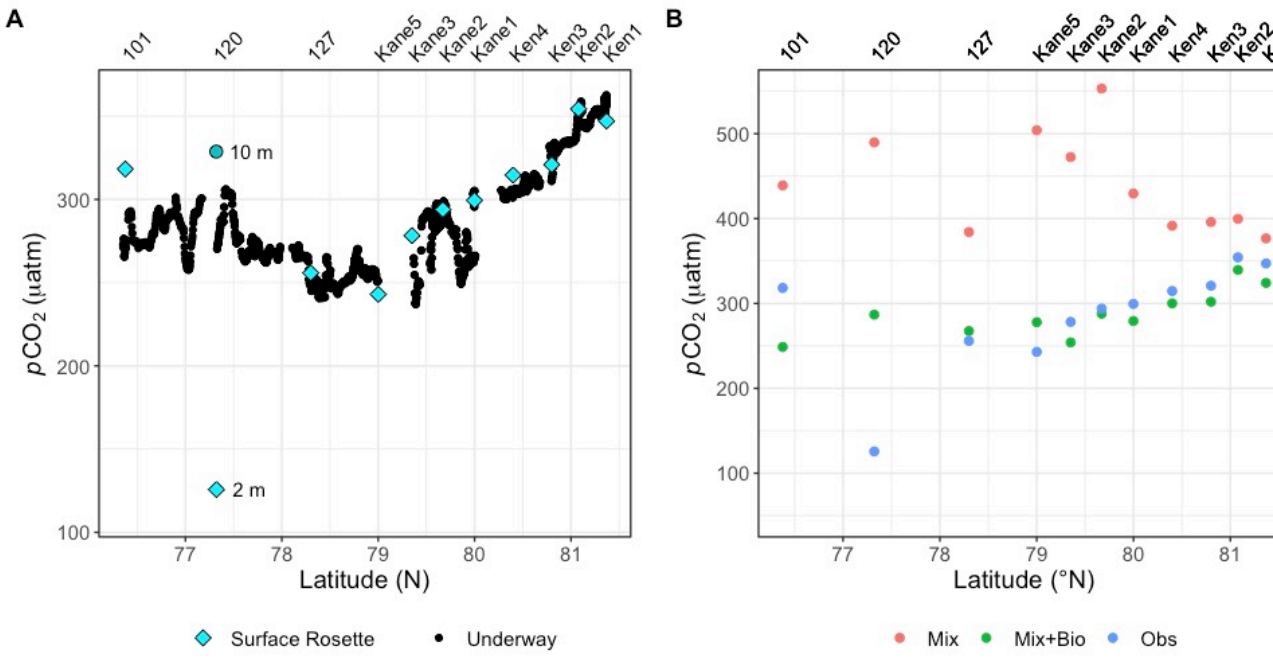


Figure 9: Trends in surface $pCO_2$ along the Nares Strait transect. (a) Surface $pCO_2$ measurements by the underway system, which sampled at 7 m depth (black dots), and calculated from DIC and TA measured in the shallowest rosette samples, at 2 m depth (blue diamonds). At station 120 the calculated $pCO_2$ is also shown for the rosette sample from 10 m depth. (b) eOMP modeled surface $pCO_2$ terms due to mixing (Mix, red dots), mixing and biology (Mix+Bio, green dots), compared against observed $pCO_2$ from surface rosette samples (blue dots, same as blue diamonds in panel a).

Further $CO_2$Sys calculations to also consider the impact of $\Delta DIC_{gas}$ estimates on surface $pCO_2$ (not shown) lead to consistent overestimates of surface $pCO_2$ compared to observational values.

Especially large surface $pCO_2$ overestimates result south of Smith Sound. This suggests that our $\Delta DIC_{gas}$ values are likely overestimates of the actual surface DIC increase due to air-sea gas exchange. There is a high relative uncertainty associated with our $\Delta DIC_{gas}$ estimates (up to 30%), and our time-integrated method of calculating $\Delta DIC_{gas}$ should be considered a maximum estimate, because the $CO_2$ equilibration time between the atmosphere and the ocean (typically several months to a year; Sarmiento & Gruber, 2006) is much longer than the residence time of surface waters transiting through Nares Strait (20 to 40 days; Münchow, 2016).

3.7 The broader picture of water mass variability in Nares Strait and the North Water

In this study we observed a water mass assembly in Kennedy Channel that resembles characteristics of the TPD and the transition zone of the Pacific-Atlantic front in the central Arctic basin. It is worth exploring how the characteristics, and nutrient availability, of the waters entering Nares Strait via the Lincoln Sea might change under a different atmospheric forcing pattern (a different Arctic Oscillation Index; AO), and what implications this might have for carbon dynamics in Nares Strait in a changing climate.

The upper ocean water masses that arrive in the Lincoln Sea vary inter-annually depending on the predominant mode of atmospheric circulation over the Arctic basin (Jackson et al., 2014; Steele et al., 2004; de Steur et al., 2013). These modes of atmospheric winds can be described by the Arctic Oscillation index (AO). To put our observations in context, during the 3 years preceding our observations on the 2014 ArcticNet cruise, the winter season (JFM) average AO was neutral to negative, and thus the TPD was likely aligned over the Lomonosov Ridge, delivering western Siberian coastal waters to the Lincoln Sea (solid red arrows, Figure 1b). We consider the winter season AO, because the cold season commonly captures the largest AO variability throughout the year (NOAA Climate Prediction Center: https://www.cpc.ncep.noaa.gov/products /precip/CWlink/daily_ao_index/ao.shtml#publication) and the JFM indices have been similarly employed in previous studies of surface water mass transport across the Arctic Ocean (Steele et al., 2004; de Steur et al., 2013).

Under a positive AO, characterized by a less expansive Beaufort Gyre, the TPD tends to be aligned over the Mendeleyev Ridge, transporting a greater proportion of Pacific-source waters from the Chukchi Sea directly towards Fram Strait. Under this atmospheric forcing scenario, the Lincoln Sea and Nares Strait are located firmly in the Pacific-sector of the Arctic Ocean, to the west of the Pacific-Atlantic front (Figure 1b). Therefore, under this forcing scenario we would expect the water mass assembly entering Nares Strait from the north to be more representative of the Canada Basin (Newton & Sotirin, 1997; Steele et al., 2004; de Steur et al., 2013). Upper water column stratification is much stronger in the Canada Basin, due to the presence of relatively low-salinity Pacific waters (both summer and winter varieties) and due to surface flow convergence within the Beaufort Gyre which acts to retain freshwater from SIM and RR in the surface mixed layer (Brown et al., 2020; Carmack et al., 2016). The perennial stratification of the Canada Basin inhibits nutrient replenishment by convective mixing with deeper water masses during the winter season (Randelhoff et al., 2020), with the upper 50 m having nitrate concentrations below 1 µM even during winter (Brown et al., 2020). The UHW layer within the Canada Basin is generally centered around 150 m depth (Alkire et al., 2021; Brown et al., 2020), slightly deeper than the UHW layer we observed in 2014 in Kennedy Channel. The UHW of the Canada Basin is also characterized by higher DIC and nutrient concentrations (DIC from 2225 to 2260 µmol $kg^{-1}$, and Si from 35 to 45 µmol $kg^{-1}$) (e.g., Alkire et al., 2021; Brown et al., 2016; Miller et al., 2014) and displays lower pH and $\Omega_{Ar}$ (7.82 ± 0.03 and 0.75 ± 0.16, respectively) (Beaupré-Laperrière et al., 2020) than in the Eurasian Basin, due to

the stronger remineralization signal downstream of the very productive Chukchi shelf (Yamamoto-Kawai et al., 2013). Were this water mass assembly to arrive in Nares Strait we would likely observe more nutrient-depleted surface waters with a higher freshwater content, and strong stratification throughout the upper water column (Coupel et al., 2015; Randelhoff et al., 2020), which could inhibit the nutrient replenishment by vertical mixing over the Kane Basin sill (Figure 2c). Under this scenario primary production in Nares Strait would be even more limited, and we could expect the waters to be more susceptible to ocean acidification, with the UHW layer likely transporting a corrosive aragonite signal ($\Omega_{Ar} < 1$) downstream into northern Baffin Bay (Azetsu-Scott et al., 2010; Yamamoto-Kawai et al., 2013).

On the other hand, under a negative AO scenario (characterized by a more expansive Beaufort Gyre with the TPD aligned over the Lomonosov Ridge) we expect the surface signal of the TPD to arrive in Nares Strait (as observed in this study), transporting with it high surface *f*CDOM from Siberian river runoff (Stedmon et al., 2021) and moderate surface nutrient concentrations. Our observations in Kennedy Channel show modest nitrate concentrations entering from the north (up to 3.5 µmol $kg^{-1}$ in PMW; Figure 3e). Charette et al. (2020) found that nitrate concentrations in the upper 50 m of the TPD in the central Arctic Ocean ranged from 0 to 8.4 µM during a similar period of neutral to negative AO (their observations are from 2015). Although these surface nitrate concentrations are still not high in comparison to those observed in the Eurasian Basin, which can reach up to 11 µM (Randelhoff et al., 2020; Brown et al., 2020), the fact remains that under a negative AO scenario Nares Strait likely receives more surface nitrate than would arrive from the Canada Basin under a positive AO. Also, under a negative AO forcing, any UHW (containing elevated nutrient concentrations) will be located at slightly shallower depths in the water column. Charette et al. (2020) observed the high-silicate UHW centered at 80 m depth underneath the TPD in the central Arctic Ocean, whereas in this study it was centered at 100 m depth in Kennedy Channel. The relatively shallow position of the UHW layer and the decreased stratification in the Eurasian Basin, compared to the Canada Basin, would make it easier for nutrients from deeper waters to be entrained into the euphotic zone by upwelling and mixing over the Kane Basin sill.

Much remains unknown about water mass transport from the WGC and variability in the NOW region (Mortensen et al., 2022). However, a number of recent modeling studies align in predicting that the strength of the WGC, and the amount of heat it transports around Baffin Bay in the SPMW layer, will likely increase in the future (Buchart et al., 2022; Castro de la Guardia et al., 2015; Gillard et al., 2020; Grivault et al., 2017). Recent paleoclimate studies of the NOW polynya region also suggest that warm periods have historically been associated with warming SPMW temperatures, further northward penetration of SPMW, and decreased productivity (Jackson et al., 2021; Ribeiro et al., 2021). In this study we observed SPMW with a temperature of 2 °C arriving in the southeastern NOW region (at approximately 76 °N; Table 1), but temperatures

of SPMW contributions farther north quickly decreased to temperatures below 0 °C as SPMW mixed with UHW and CBAW (Figures 2 and 4). More observational studies are needed to inform on the changing strength and heat content of the WGC and its influence on the NOW region.

## 4 Summary and Conclusions

In this study, we have described the interaction of water masses entering Nares Strait from the north (Kennedy Channel) and south (the North Water polynya region of northern Baffin Bay) using a series of chemical tracers and an extended optimum multi-parameter (eOMP) analysis. Our tracer observations in Kennedy Channel display a Polar Mode water (PMW) characterized by high fCDOM, near freezing temperatures and low salinity (31.4), indicating the arrival of Siberian shelf waters in Nares Strait. These surface waters were likely transported across the Arctic basin by the Transpolar drift (TPD). Underneath the PMW, we find a slightly diluted layer of Upper Halocline water (UHW) of partial Pacific origin (as indicated by ANP values of  0.5; Newton et al., 2013), displaying silicate concentrations up to 18 µmol $kg^{-1}$, and centered at 100 m depth. These upper water column characteristics indicate that our sampling region in Kennedy Channel likely received waters influenced by the TPD and the Pacific-Atlantic front. The deep water column in Kennedy Channel contains Canada Basin Atlantic water (CBAW), with a relatively warm temperature (T = 0.36 °C) compared to the other Arctic-outflow water masses.

Across the North Water polynya region of northern Baffin Bay we observe an additional two water masses entering Nares Strait from the southeast. The upper water column is dominated by Baffin Bay Polar water (BBPW), a winter mode water formed somewhere in eastern Baffin Bay (Mortensen et al., 2022; Rysgaard et al., 2020), characterized by a near-surface temperature minimum close to the freezing point and a salinity of approximately 33.5. Centered at 300 m depth we also observe a relatively warm (T = 2 °C) and saline ($S_P$ = 34.3) Subpolar Mode Water (SPMW) layer transiting northwards. SPMW is also characterized by high nutrient and low DO concentrations, suggesting a history of organic matter remineralization, leading to the lowest observed $pH_T$ and calcium carbonate saturation states ($pH_T$ = 7.85, $\Omega_{Ca}$ = 1.49, $\Omega_{Ar}$ = 0.94) of any water mass in our study region.

The results of our eOMP analysis document the interaction of all these source water masses throughout Nares Strait, and the effects of water mass mixing and biological processes on the DIC budget of the region. We find a great degree of mixing in Kane Basin, driven by the presence of a shallow sill (220 m depth), which forces upwelling and vertical mixing between the UHW and CBAW layers from the north, and the BBPW and SPMW layers from the south. Fractions of BBPW up to 45% were observed in Kane Basin, along with relatively smaller fractions of SPMW (up to 15%) The role of water mass mixing clearly dominates the DIC budget of the region, although a modest phytoplankton bloom in Kane Basin is found to play a key role in decreasing surface $pCO_2$ concentrations throughout Nares Strait. We do not observe any significant respiration signal

at depth within Nares Strait, suggesting that there is either too little primary production occurring to generate a detectable respiration signal from sinking biomass, or the currents may be too fast in Nares Strait to allow enough time for sinking particles to accumulate and remineralize within the strait (surface waters only take 20 to 40 days to flow through Nares Strait; Münchow, 2016). We do observe a respiration signal at depth in the NOW region ($DIC_{bio}$ as high as 30 µmol $kg^{-1}$), associated with high SPMW fractions, implying that the respiration signal is derived from organic matter transported with this water mass from the West Greenland shelf. Air-sea gas exchange is found to play a minor role in the surface carbon dynamics in this region, although atmospheric $CO_2$ uptake may be responsible for a slight increase in surface $pCO_2$ south of Smith Sound (at stations 120 and 101), where wind speeds were high and we observed a coincident increase in AOU, suggesting the uptake of atmospheric $O_2$ as well.

These results represent only one snapshot in time of the water mass characteristics in Nares Strait, a waterway that is subject to large interannual variability in water mass fluxes from the Arctic Ocean (Jackson et al., 2014; de Steur et al., 2013). As climate change affects the Arctic Ocean and Baffin Bay, it is likely that greater freshwater inputs from melting sea ice, glaciers, and rivers will further increase freshwater content in this area, leading to enhanced stratification of the water column and further limiting nutrient availability for primary production (Bergeron & Tremblay, 2014; Blais et al., 2017). Our observations in Kennedy Channel show that there is already very limited nutrient availability in surface waters from the TPD, and if a different surface water mass were to arrive from the Canada Basin, nutrient availability would likely be even more limited (Brown et al., 2020; Coupel et al., 2015; Randelhoff et al., 2020). At the same time, the northward transport of water masses from the West Greenland shelf may increase in the future with a strengthening of the WGC (Buchart et al., 2022; Castro de la Guardia et al., 2015; Jackson et al., 2021), and will perhaps become the dominant source of surface nutrients to the NOW region, despite also being influenced by increasing freshwater inputs.

## Data Availability

All meteorological tower measurements 2014 can be found in the Polar Data Catalogue (CCIN: 11872 and 12063), as well as chlorophyll a concentrations (CCIN: 11843 and 12028). All underway $pCO_2$ data and bottle measurements of DIC and TA are available through the National Centers for Environmental Information (NCEI) Ocean Archive (NCEI Accession 0167322). NCEP NARR 8 times daily wind velocity measurements (U-wind and V-wind individual observations at the 10 m level) are available at https://psl.noaa.gov/data/gridded/data.narr.html. Some figures in this paper were produced using Ocean Data View (Schlitzer, 2020). Some of the data presented herein were collected by the Canadian research icebreaker CCGS Amundsen and made available by the Amundsen Science program (https://amundsenscience.com/data/data-access/), which was supported by

the Canada Foundation for Innovation and Natural Sciences and Engineering Research Council of Canada. The views expressed in this publication do not necessarily represent the views of Amundsen Science or that of its partners.

Acknowledgements

Thanks to the captain and crew of the CCGS *Amundsen*, as well as Keith Levesque, Emmelia Stainton, and Sebastian Luque for logistical support. We are especially thankful to Vickie Irish and Jacoba Mol for assistance with field sampling; Marty Davelaar for logistical assistance and analyzing all the DIC and TA samples; Gabrielle Deslongchamps and Jonathan Gagnon for nutrient sample collection and analysis, and the Amundsen Science technicians for the collection and processing of CTD data. A special thank you to Ashley Dinauer for providing the base MATLAB code for the eOMP analysis and helpful guidance. Financial support for this work was provided by ArcticNet, NSERC's Canada Postgraduate Scholarships Doctoral (PGS D) and Discovery Grant Programs, Fisheries and Oceans Canada, and by the CERC program at the University of Manitoba (D. Dahl-Jensen).

References

Ahmed, M. M. M., Else, B. G. T., Capelle, D., Miller, L. A., & Papakyriakou, T. (2020). Underestimation of surface pCO2 and air-sea $CO_2$ fluxes due to freshwater stratification in an Arctic shelf sea, Hudson Bay. *Elementa*, *8*(1). https://doi.org/10.1525/elementa.084Alkire, M. B., Falkner, K. K., Boyd, T., & Macdonald, R. W. (2010). Sea ice melt and meteoric water distributions in Nares Strait, Baffin Bay, and the Canadian Arctic Archipelago. *Journal of Marine Research*, *68*(6), 767–798.Alkire, M. B., Rember, R., & Polyakov, I. (2021). The Pacific-Atlantic Front in the East Siberian Sea of the Arctic Ocean. In *The Handbook of Environmental Chemistry*. Springer, Berlin, Heidelberg. https://doi.org/10.1007/698_2021_795Amundsen Science Data Collection. (2018). CTD data collected by the CCGS Amundsen in the Canadian Arctic. ArcticNet Inc., Québec, Canada. Processed data. Version 1, Release 2. Archived at www.polardata.ca, Canadian Cryospheric Information Network (CCIN), Waterloo, Canada. https://doi.org/10.5884/12713. Accessed January 2020.Anderson, L. G., Andersson, P. S., Björk, G., Jones, E. P., Jutterström, S., & Wåhlström, I. (2013). Source and formation of the upper halocline of the Arctic Ocean. *Journal of Geophysical Research: Oceans*, *118*, 410–421. https://doi.org/10.1029/2012JC008291Anderson, L. G., Björk, G., Holby, O., Jutterström, S., Magnus Mörth, C., O'Regan, M., et al. (2017). Shelf-Basin interaction along the East Siberian Sea. *Ocean Science*, *13*(2), 349–363. https://doi.org/10.5194/os-13-349-2017Azetsu-Scott, K., Clarke, A., Falkner, K., Hamilton, J., Jones, E. P., Lee, C., et al. (2010). Calcium carbonate saturation states in the waters of the Canadian Arctic Archipelago and the Labrador Sea. *Journal of Geophysical Research: Oceans*, *115*(C11021). https://doi.org/10.1029/2009JC005917Azetsu-Scott, K., Petrie, B., Yeats, P., & Lee, C. (2012). Composition and fluxes of freshwater through Davis Strait using multiple chemical tracers. *Journal of Geophysical Research*, *117*(C12),

C12011. https://doi.org/10.1029/2012JC008172Bâcle, J., Carmack, E. C., & Ingram, R. G. (2002). Water column structure and circulation under the North Water during spring transition: April-July 1998. *Deep-Sea Research Part II: Topical Studies in Oceanography*, *49*, 4907–4925. https://doi.org/10.1016/S0967-0645(02)00170-4Barber, D. G., Babb, D. G., Ehn, J. K., Chan, W., Matthes, L., Dalman, L. A., et al. (2018). Increasing Mobility of High Arctic Sea Ice Increases Marine Hazards Off the East Coast of Newfoundland. *Geophysical Research Letters*, *45*, 2370–2379. https://doi.org/10.1002/2017GL076587Bauch, D., van der Loeff, M. R., Andersen, N., Torres-Valdes, S., Bakker, K., & Abrahamsen, E. P. (2011). Origin of freshwater and polynya water in the Arctic Ocean halocline in summer 2007. *Progress in Oceanography*, *91*, 482–495. https://doi.org/10.1016/j.pocean.2011.07.017Beaupré-Laperrière, A., Mucci, A., & Thomas, H. (2020). The recent state and variability of the carbonate system of the Canadian Arctic Archipelago and adjacent basins in the context of ocean acidification. *Biogeosciences*, *17*, 3923–3942. https://doi.org/10.5194/bg-17-3923-2020Bergeron, M., & Tremblay, J.-É. (2014). Shifts in biological productivity inferred from nutrient drawdown in the southern Beaufort Sea (2003-2011) and northern Baffin Bay (1997-2011), Canadian Arctic. *Geophysical Research Letters*, *41*, 3979–3987. https://doi.org/10.1002/2014GL059649Blais, M., Ardyna, M., Gosselin, M., Dumont, D., Bélanger, S., Tremblay, J.-É., et al. (2017). Contrasting interannual changes in phytoplankton productivity and community structure in the coastal Canadian Arctic Ocean. *Limnology and Oceanography*, *62*(6), 2480–2497. https://doi.org/10.1002/lno.10581Broecker, W. S. (1974). "NO", a conservative water-mass tracer. *Earth and Planetary Science Letters*, *23*(1), 100–107. https://doi.org/10.1016/0012-821X(74)90036-3Brown, K. A., McLaughlin, F., Tortell, P. D., Yamamoto-Kawai, M., & Francois, R. (2016). Sources of dissolved inorganic carbon to the Canada Basin halocline: A multitracer study. *Journal of Geophysical Research: Oceans*, *121*. https://doi.org/10.1002/2015JC011535Brown, K. A., Holding, J. M., & Carmack, E. C. (2020). Understanding Regional and Seasonal Variability Is Key to Gaining a Pan-Arctic Perspective on Arctic Ocean Freshening. *Frontiers in Marine Science*, *7*(August), 1–25. https://doi.org/10.3389/fmars.2020.00606Buchart, L., Castro de la Guardia, L., Xu, Y., Ridenour, N., Marson, J. M., Deschepper, I., et al. (2022). Future Climate Scenarios for Northern Baffin Bay and the Pikialasorsuaq ( North Water Polynya ) Region. *Atmosphere-Ocean*, 1–22. https://doi.org/10.1080/07055900.2022.2067028Burgers, T. M., Miller, L. A., Thomas, H., Else, B. G. T., Gosselin, M., & Papakyriakou, T. (2017). Surface Water $pCO_2$ variations and sea-air CO2 fluxes during summer in the eastern Canadian Arctic. *Journal of Geophysical Research: Oceans*, *122*, 9663–9678. https://doi.org/10.1002/2017JC013250Burgers, T. M., Tremblay, J.-É., Else, B. G. T., & Papakyriakou, T. N. (2020). Estimates of net community production from multiple approaches surrounding the spring ice-edge bloom in Baffin Bay. *Elementa: Science of the Anthropocene*, *8*(1). https://doi.org/10.1525/elementa.013Carmack, E. C., Yamamoto-

Kawai, M., Haine, T. W. N., Bacon, S., Bluhm, B. A., Lique, C., et al. (2016). Freshwater and its role in the Arctic Marine System: Sources, disposition, storage, export, and physical and biogeochemical consequences in the Arctic and global oceans. *Journal of Geophysical Research: Biogeosciences*, *121*, 675–717. https://doi.org/10.1002/2015JG003140Castro de la Guardia, L., Hu, X., & Myers, P. G. (2015). Potential positive feedback between Greenland Ice Sheet melt and Baffin Bay heat content on the west Greenland shelf. *Geophysical Research Letters*, *42*, 4922–4930. https://doi.org/10.1002/2015GL064626Charette, M. A., Kipp, L. E., Jensen, L. T., Dabrowski, J. S., Whitmore, L. M., Fitzsimmons, J. N., et al. (2020). The Transpolar Drift as a Source of Riverine and Shelf-Derived Trace Elements to the Central Arctic Ocean. *Journal of Geophysical Research: Oceans*, *125*(5). https://doi.org/10.1029/2019JC015920Coupel, P., Ruiz-Pino, D., Sicre, M. A., Chen, J. F., Lee, S. H., Schiffrine, N., et al. (2015). The impact of freshening on phytoplankton production in the Pacific Arctic Ocean. *Progress in Oceanography*, *131*, 113–125. https://doi.org/10.1016/j.pocean.2014.12.003Curry, B., Lee, C. M., Petrie, B., Moritz, R. E., & Kwok, R. (2014). Multiyear Volume, Liquid Freshwater, and Sea Ice Transports through Davis Strait, 2004–10*. *Journal of Physical Oceanography*, *44*(4), 1244–1266. https://doi.org/10.1175/JPO-D-13-0177.1Dickson, A. G. (1990). Standard potential of the reaction: AgCl(s) + $12H_2$(g) = Ag(s) + HCl(aq), and the standard acidity constant of the ion $HSO_4^-$ in synthetic sea water from 273.15 to 318.15 K. *Chem. Thermodyn.*, *22*, 113–127.Dickson, A. G., Sabine, C. L., & Christian, J. R. (2007). Guide to best practices for ocean $CO_2$ measurements. *PICES Special Publication*, *3*, p191. https://doi.org/10.1159/000331784Dinauer, A., & Mucci, A. (2018). Distinguishing between physical and biological controls on the spatial variability of $pCO_2$: A novel approach using OMP water mass analysis (St. Lawrence, Canada). *Marine Chemistry*, *204*(April), 107–120. https://doi.org/10.1016/j.marchem.2018.03.007Dodd, P. A., Rabe, B., Hansen, E., Falck, E., MacKensen, A., Rohling, E., et al. (2012). The freshwater composition of the Fram Strait outflow derived from a decade of tracer measurements. *Journal of Geophysical Research: Oceans*, *117*(11), 1–26. https://doi.org/10.1029/2012JC008011Dong, Y., Yang, M., Bakker, D. C. E., Liss, P. S., Kitidis, V., Brown, I., et al. (2021). Near-Surface Stratification Due to Ice Melt Biases Arctic Air-Sea $CO_2$ Flux Estimates. *Geophysical Research Letters*, *48*, e2021GL095266. https://doi.org/10.1029/2021GL095266Eegeesiak, O., Aariak, E., & Kleist, K. V. (2017). *People of the Ice Bridge: The Future of the Pikialasorsuaq. Pikialasorsuaq Commission.* Ottawa.Gillard, L. C., Hu, X., Myers, P. G., Ribergaard, M. H., & Lee, C. M. (2020). Drivers for Atlantic-origin waters abutting Greenland. *Cryosphere*, *14*, 2729–2753. https://doi.org/10.5194/tc-14-2729-2020Gonçalves-Araujo, R., Granskog, M. A., Bracher, A., Azetsu-Scott, K., Dodd, P. A., & Stedmon, C. A. (2016). Using fluorescent dissolved organic matter to trace and distinguish the origin of Arctic surface waters. *Scientific Reports*, *6*, 33978. https://doi.org/10.1038/srep33978Granskog, M. A., Stedmon, C. A., Dodd, P. A., Amon, R. M. W., Pavlov, A. K., De Steur, L., & Hansen, E. (2012).

Characteristics of colored dissolved organic matter (CDOM) in the Arctic outflow in the Fram Strait: Assessing the changes and fate of terrigenous CDOM in the Arctic Ocean. *Journal of Geophysical Research*, *117*, C12021. https://doi.org/10.1029/2012JC008075Grivault, N., Hu, X., & Myers, P. G. (2017). Evolution of Baffin Bay Water Masses and Transports in a Numerical Sensitivity Experiment under Enhanced Greenland Melt. *Atmosphere - Ocean*, *55*(3), 169–194. https://doi.org/10.1080/07055900.2017.1333950Hamilton, A. K., Mueller, D., & Laval, B. E. (2021). Ocean Modification and Seasonality in a Northern Ellesmere Island Glacial Fjord Prior to Ice Shelf Breakup: Milne Fiord. *Journal of Geophysical Research: Oceans*, *126*. https://doi.org/10.1029/2020jc016975Hansen, H. P., & Koroleff, F. (1999). Determination of nutrients. In K. Grasshoff, K. Kremling, & M. Ehrhardt (Eds.), *Methods of seawater analysis* (3rd ed., pp. 159–228). Weinheim, Germany: Wiley-VCH. https://doi.org/10.1002/9783527613984.ch10van Heuven, S., Pierrot, D., Rae, J. W. B., Lewis, E., & Wallace, D. W. R. (2011). MATLAB program developed for $CO_2$ system calculations. Oak Ridge: US Department of Energy: ORML/CDIAC-105b. Carbon Dioxide Information Analysis Center. https://doi.org/doi: 10.3334/CDIAC/otg.CO2SYS_MATLAB_v1.1Holmes, R. M., Aminot, A., Kérouel, R., Hooker, B. A., & Peterson, B. J. (1999). A simple and precise method for measuring ammonium in marine and freshwater ecosystems. *Canadian Journal of Fisheries and Aquatic Sciences*, *56*, 1801–1808. https://doi.org/10.1139/f99-128Jackson, J. M., Lique, C., Alkire, M., Steele, M., Lee, C. M., Smethie, W. M., & Schlosser, P. (2014). On the waters upstream of Nares Strait, Arctic Ocean, from 1991 to 2012. *Continental Shelf Research*, *73*, 83–96. https://doi.org/10.1016/j.csr.2013.11.025Jackson, R., Kvorning, A. B., Limoges, A., Georgiadis, E., Olsen, S. M., Tallberg, P., et al. (2021). Holocene polynya dynamics and their interaction with oceanic heat transport in northernmost Baffin Bay. *Scientific Reports*, *11*, 10095. https://doi.org/10.1038/s41598-021-88517-9Jones, E. P., & Anderson, L. G. (1986). On the origin of the chemical properties of the Arctic Ocean halocline. *Journal of Geophysical Research: Oceans*, *91*(C9), 10759–10767. https://doi.org/10.1029/jc091ic09p10759Jones, E Peter, Anderson, L. G., & Swift, J. H. (1998). Distribution of Atlantic and Pacific waters in the upper Arctic Ocean: Implications for circulation. *Geophysical Research Letters*, *25*(6), 765–768. https://doi.org/10.1029/98gl00464Kwok, R., Pedersen, L. T., Gudmandsen, P., & Pang, S. S. (2010). Large sea ice outflow into the Nares Strait in 2007. *Geophysical Research Letters*, *37*, L03502. https://doi.org/10.1029/2009GL041872Lansard, B., Mucci, A., Miller, L. A., Macdonald, R. W., & Gratton, Y. (2012). Seasonal variability of water mass distribution in the southeastern Beaufort Sea determined by total alkalinity and $^{18}O$. *Journal of Geophysical Research*, *117*, C03003. https://doi.org/10.1029/2011JC007299Lee, K., Kim, T.-W., Byrne, R. H., Millero, F. J., Feely, R. A., & Liu, Y.-M. (2010). The universal ratio of boron to chlorinity for the North Pacific and North Atlantic oceans. *Geochimica et Cosmochimica Acta*, *74*(6), 1801–1811. https://doi.org/10.1016/j.gca.2009.12.027Lobb, J., Weaver, A. J., Carmack,

E. C., & Ingram, R. G. (2003). Structure and mixing across an Arctic/Atlantic front in northern Baffin Bay. *Geophysical Research Letters*, *30*(16), 1833. https://doi.org/10.1029/2003GL017755Lueker, T. J., Dickson, A. G., & Keeling, C. D. (2000). Ocean $pCO_2$ calculated from dissolved inorganic carbon, alkalinity, and equations for K1 and K2: validation based on laboratory measurements of $CO_2$ in gas and seawater at equilibrium. *Marine Chemistry*, *70*, 105–119.Marchese, C., Albouy, C., Tremblay, J.-É., Dumont, D., D'Ortenzio, F., Vissault, S., & Bélanger, S. (2017). Changes in phytoplankton bloom phenology over the North Water (NOW) polynya: a response to changing environmental conditions. *Polar Biology*, *40*, 1721–1737. https://doi.org/10.1007/s00300-017-2095-2McLaughlin, F. A., Carmack, E. C., Macdonald, R. W., & Bishop, J. K. B. (1996). Physical and geochemical properties across the Atlantic / Pacific water mass front in the southern Canadian Basin. *Journal of Geophysical Research*, *101*(C1), 1183–1197. https://doi.org/https://doi.org/10.1029/95JC02634Melling, H., Gratton, Y., & Ingram, G. (2001). Ocean circulation within the North Water polynya of Baffin Bay. *Atmosphere - Ocean*, *39*(3), 301–325. https://doi.org/10.1080/07055900.2001.9649683Miller, L. A., Papakyriakou, T. N., Collins, R. E., Deming, J. W., Ehn, J. K., MacDonald, R. W., et al. (2011). Carbon dynamics in sea ice: A winter flux time series. *Journal of Geophysical Research: Oceans*, *116*, C02028. https://doi.org/10.1029/2009JC006058Miller, L. A., Macdonald, R. W., Mclaughlin, F., Mucci, A., Yamamoto-Kawai, M., Giesbrecht, K. E., et al. (2014). Changes in the marine carbonate system of the western Arctic: patterns in a rescued data set. *Polar Research*, *33*(1), 20577. https://doi.org/10.3402/polar.v33.20577Miller, L. A., Burgers, T. M., Burt, W. J., Granskog, M. A., & Papakyriakou, T. N. (2019). Air-Sea $CO_2$ Flux Estimates in Stratified Arctic Coastal Waters : How Wrong Can We Be ? *Geophysical Research Letters*, *46*, 235–243. https://doi.org/10.1029/2018GL080099Moore, G. W. K., Schweiger, A., Zhang, J., & Steele, M. (2019). Spatiotemporal Variability of Sea Ice in the Arctic's Last Ice Area. *Geophysical Research Letters*, *46*, 11237–11243. https://doi.org/10.1029/2019GL083722Morison, J., Kwok, R., Peralta-Ferriz, C., Alkire, M., Rigor, I., Andersen, R., & Steele, M. (2012). Changing Arctic Ocean freshwater pathways. *Nature*, *481*, 66–70. https://doi.org/10.1038/nature10705Mortensen, J., Rysgaard, S., Winding, M. H. S., Arendt, K. E., Lund, H., Stuart-Lee, A. E., & Meire, L. (2022). Multidecadal Water Mass Dynamics on the West Greenland Shelf. *Journal of Geophysical Research: Oceans*, *127*. https://doi.org/10.1029/2022JC018724Münchow, A. (2016). Volume and freshwater flux observations from Nares Strait to the west of Greenland at daily time scales from 2003 to 2009. *Journal of Physical Oceanography*, *46*(1), 141–157. https://doi.org/10.1175/JPO-D-15-0093.1Münchow, A., Melling, H., & Falkner, K. K. (2006). An observational estimate of volume and freshwater flux leaving the Arctic Ocean through Nares Strait. *Journal of Physical Oceanography*, *36*(11), 2025–2041. https://doi.org/10.1175/JPO2962.1Münchow, A., Falkner, K. K., & Melling, H. (2007). Spatial continuity of measured

seawater and tracer fluxes through Nares Strait, a dynamically wide channel bordering the Canadian Archipelago. *Journal of Marine Research*, *65*, 759–788. https://doi.org/10.1357/002224007784219048Münchow, A., Falkner, K. K., & Melling, H. (2015). Baffin Island and West Greenland Current Systems in northern Baffin Bay. *Progress in Oceanography*, *132*, 305–317. https://doi.org/10.1016/j.pocean.2014.04.001Mundy, C. J., Gosselin, M., Ehn, J. K., Belzile, C., Poulin, M., Alou, E., et al. (2011). Characteristics of two distinct high-light acclimated algal communities during advanced stages of sea ice melt. *Polar Biology*, *34*, 1869–1886. https://doi.org/10.1007/s00300-011-0998-xMyers, P. G., Donnelly, C., & Ribergaard, M. H. (2009). Structure and variability of the West Greenland Current in Summer derived from 6 repeat standard sections. *Progress in Oceanography*, *80*(1–2), 93–112. https://doi.org/10.1016/j.pocean.2008.12.003Myers, P. G., Castro de la Guardia, L., Fu, C., Gillard, L. C., Grivault, N., Hu, X., et al. (2021). Extreme High Greenland Blocking Index Leads to the Reversal of Davis and Nares Strait Net Transport Toward the Arctic Ocean. *Geophysical Research Letters*, *48*. https://doi.org/10.1029/2021GL094178Newton, J. L., & Sotirin, B. J. (1997). Boundary undercurrent and water mass changes in the Lincoln Sea. *Journal of Geophysical Research: Oceans*, *102*(C2), 3393–3403.Newton, R., Schlosser, P., Mortlock, R., Swift, J., & MacDonald, R. (2013). Canadian Basin freshwater sources and changes: Results from the 2005 Arctic Ocean Section. *Journal of Geophysical Research: Oceans*, *118*, 2133–2154. https://doi.org/10.1002/jgrc.20101Nishino, S., Itoh, M., Williams, W. J., & Semiletov, I. (2013). Shoaling of the nutricline with an increase in near-freezing temperature water in the Makarov Basin. *Journal of Geophysical Research: Oceans*, *118*, 635–649. https://doi.org/10.1029/2012JC008234Nitishinsky, M., Anderson, L. G., & Hölemann, J. A. (2007). Inorganic carbon and nutrient fluxes on the Arctic Shelf. *Continental Shelf Research*, *27*, 1584–1599. https://doi.org/10.1016/j.csr.2007.01.019Orr, J. C., Epitalon, J.-M., Dickson, A. G., & Gattuso, J.-P. (2018). Routine uncertainty propagation for the marine carbon dioxide system. *Marine Chemistry*, *207*(June), 84–107. https://doi.org/10.1016/j.marchem.2018.10.006Östlund, H. G., & Hut, G. (1984). Arctic Ocean water mass balance from isotope data. *Journal of Geophysical Research: Oceans*, *89*(C4), 6373–6381. https://doi.org/10.1029/JC089iC04p06373Peralta-Ferriz, C., & Woodgate, R. A. (2015). Seasonal and interannual variability of pan-Arctic surface mixed layer properties from 1979 to 2012 from hydrographic data, and the dominance of stratification for multiyear mixed layer depth shoaling. *Progress in Oceanography*, *134*, 19–53. https://doi.org/10.1016/j.pocean.2014.12.005Pierrot, D., Neill, C., Sullivan, K., Castle, R., Wanninkhof, R., Lüger, H., et al. (2009). Recommendations for autonomous underway $pCO_2$ measuring systems and data-reduction routines. *Deep-Sea Research Part II*, *56*, 512–522. https://doi.org/10.1016/j.dsr2.2008.12.005Randelhoff, A., Oziel, L., Massicotte, P., Bécu, G., Galí, M., Lacour, L., et al. (2019). The evolution of light and vertical mixing across a phytoplankton ice-edge bloom. *Elementa: Science of the Anthropocene*, *7*, 20. https://doi.org/10.1525/elementa.357Randelhoff,

A., Holding, J., Janout, M., Sejr, M. K., Babin, M., Tremblay, J. É., & Alkire, M. B. (2020). Pan-Arctic Ocean Primary Production Constrained by Turbulent Nitrate Fluxes. *Frontiers in Marine Science*, *7*(150). https://doi.org/10.3389/fmars.2020.00150Ribeiro, S., Limoges, A., Massé, G., Johansen, K. L., Colgan, W., Weckström, K., et al. (2021). Vulnerability of the North Water ecosystem to climate change. *Nature Communications*, *12*, 4475. https://doi.org/10.1038/s41467-021-24742-0Rudels, B. (2009). Arctic ocean circulation. In J. H. Steele, S. A. Thorpe, & K. K. Turekian (Eds.), *Encyclopedia of Ocean Sciences* (pp. 211–225). Academic Press. https://doi.org/https://doi.org/10.1016/B978-012374473-9.00601-9Rudels, B., Jones, E. P., Schauer, U., & Eriksson, P. (2004). Atlantic sources of the Arctic Ocean surface and halocline waters. *Polar Research*, *23*(2), 181–208. https://doi.org/10.1029/2001JC001141.MacKinnonRyan, P. A., & Münchow, A. (2017). Sea ice draft observations in Nares Strait from 2003 to 2012. *Journal of Geophysical Research: Oceans*, *122*, 3057–3080. https://doi.org/10.1002/2016JC011966Rysgaard, S., Boone, W., Carlson, D., Sejr, M. K., Bendtsen, J., Juul-Pedersen, T., et al. (2020). An updated view on water masses on the pan-West Greenland continental shelf and their link to proglacial fjords. *Journal of Geophysical Research: Oceans*, *125*. https://doi.org/10.1029/2019jc015564Rysgaard, Søren, Glud, R. N., Sejr, M. K., Bendtsen, J., & Christensen, P. B. (2007). Inorganic carbon transport during sea ice growth and decay: A carbon pump in polar seas. *Journal of Geophysical Research*, *112*, C03016. https://doi.org/10.1029/2006JC003572Rysgaard, Søren, Glud, R. N., Sejr, M. K., Blicher, M. E., & Stahl, H. J. (2008). Denitrification activity and oxygen dynamics in Arctic sea ice. *Polar Biology*, *31*(5), 527–537. https://doi.org/10.1007/s00300-007-0384-xSarmiento, J. L., & Gruber, N. (2006). *Ocean Biogeochemical Dynamics*. Princeton: Princeton University Press.Schlitzer, R. (2020). Ocean Data View. https://doi.org/https://odv.awi.deSemiletov, I., Dudarev, O., Luchin, V., Charkin, A., Shin, K.-H., & Tanaka, N. (2005). The East Siberian Sea as a transition zone between Pacific-derived waters and Arctic shelf waters. *Geophysical Research Letters*, *32*, L10614. https://doi.org/10.1029/2005GL022490Stedmon, C. A., Amon, R. M. W., Bauch, D., Bracher, A., Gonçalves-Araujo, R., Hoppmann, M., et al. (2021). Insights Into Water Mass Origins in the Central Arctic Ocean From In-Situ Dissolved Organic Matter Fluorescence. *Journal of Geophysical Research: Oceans*, *126*, e2021JC017407. https://doi.org/10.1029/2021JC017407Steele, M., Morison, J., Ermold, W., Rigor, I., & Ortmeyer, M. (2004). Circulation of summer Pacific halocline water in the Arctic Ocean. *Journal of Geophysical Research*, *109*, C02027. https://doi.org/10.1029/2003JC002009de Steur, L., Steele, M., Hansen, E., Morison, J., Polyakov, I., Olsen, S. M., et al. (2013). Hydrographic changes in the Lincoln Sea in the Arctic Ocean with focus on an upper ocean freshwater anomaly between 2007 and 2010. *Journal of Geophysical Research: Oceans*, *118*, 4699–4715. https://doi.org/10.1002/jgrc.20341Tang, C. C. L., Ross, C. K., Yao, T., Petrie, B., DeTracey, B. M., & Dunlap, E. (2004). The circulation, water masses and sea-ice of Baffin Bay. *Progress in Oceanography*, *63*, 183–228.

https://doi.org/10.1016/j.pocean.2004.09.005Tomczak, M, & Large, D. (1989). Optimim Multiparameter Analysis of Mixing in the Thermocline of the Eastern Indian Ocean. *Journal of Geophysical Research: Oceans*, *94*(Cll), 15141–16149. https://doi.org/10.1029/JC094iC11p16141Tomczak, Matthias. (1981). A multi-parameter extension of temperature/salinity diagram techniques for the analysis of non-isopycnal mixing. *Progress in Oceanography*, *10*, 147–171. https://doi.org/10.1016/0079-6611(81)90010-0Tremblay, J.-É., Gratton, Y., Carmack, E. C., Payne, C. D., & Price, N. M. (2002). Impact of the large-scale Arctic circulation and the North Water Polynya on nutrient inventories in Baffin Bay. *Journal of Geophysical Research*, *107*, C8. https://doi.org/10.1029/2000JC000595Tremblay, J.-É., Anderson, L. G., Matrai, P., Coupel, P., Bélanger, S., Michel, C., & Reigstad, M. (2015). Global and regional drivers of nutrient supply, primary production and $CO_2$ drawdown in the changing Arctic Ocean. *Progress in Oceanography*, *139*, 171–196. https://doi.org/10.1016/j.pocean.2015.08.009Vincent, R. F. (2019). A Study of the North Water Polynya Ice Arch using Four Decades of Satellite Data. *Scientific Reports*, *9*, 20278. https://doi.org/10.1038/s41598-019-56780-6Wang, X., Zhao, J., Lobanov, V. B., Kaplunenko, D., Rudykh, Y. N., He, Y., & Chen, X. (2021). Distribution and Transport of Water Masses in the East Siberian Sea and Their Impacts on the Arctic Halocline. *Journal of Geophysical Research: Oceans*, *126*. https://doi.org/10.1029/2020JC016523Wanninkhof, R. (2014). Relationship between wind speed and gas exchange over the ocean revisited. *Limnology and Oceanography: Methods*, *12*, 351–362. https://doi.org/https://doi.org/10.4319/lom.2014.12.351Weiss, R. F. (1974). Carbon dioxide in water and seawater: the solubility of a non-ideal gas. *Marine Chemistry*, *2*(3), 203–215. https://doi.org/10.1016/0304-4203(74)90015-2Yamamoto-Kawai, M., McLaughlin, F. A., Carmack, E. C., Nishino, S., & Shimada, K. (2008). Freshwater budget of the Canada Basin, Arctic Ocean, from salinity, $^{18}O$, and nutrients. *Journal of Geophysical Research: Oceans*, *113*, C01007. https://doi.org/10.1029/2006JC003858Yamamoto-Kawai, Michiyo, McLaughlin, F., & Carmack, E. (2013). Ocean acidification in the three oceans surrounding northern North America. *Journal of Geophysical Research: Oceans*, *118*(11), 6274–6284. https://doi.org/10.1002/2013JC009157